Interaction of vorticity, rate-of-strain, and scalar gradient in stratified homogeneous sheared turbulence

P. J. Diamessis and K. K. Nomura[a)]
Department of Mechanical and Aerospace Engineering, University of California at San Diego, La Jolla, California 92093-0411

(Received 20 October 1999; accepted 25 January 2000)

The structure and dynamics of stably stratified homogeneous sheared turbulence is investigated in terms of the triadic interaction of vorticity ω, rate-of-strain S, and scalar (density fluctuation) gradient $\mathbf{G}\equiv\nabla\rho'$. Results of direct numerical simulations are presented. Due to the presence of the mean velocity and scalar gradients, distinct directional preferences develop which affect the dynamics of the flow. The triadic interaction is described in terms of the direct coupling of primary mechanism pairs and influential secondary effects. Interaction of ω and S is characterized by the coupling of vortex stretching and locally-induced rotation of the S axes. Due to the intrinsic directionality of baroclinic torque, the generated ω acts to impede S axes rotation. Interaction of ω and $\mathbf{G}$ involves an inherent negative feedback between baroclinic torque and reorientation of $\mathbf{G}$ by ω. This causes baroclinic torque to act as a sink which promotes decay of ω^2. Interaction of S and $\mathbf{G}$ is characterized by a positive feedback between differential acceleration and gradient amplification by compressive straining which promotes persistence in vertical $\mathbf{G}$. In high-amplitude, rotation-dominated regions of the flow, differential acceleration effects enhance the attenuation of vertical ω while shear and baroclinic torque tend to maintain horizontal ω. This leads to a predominance of horizontal ω in these regions which manifests itself as *collapsed* vortex structures. As the flow develops, the third invariant of the velocity gradient tensor tends towards zero indicating locally two-dimensional flow. [S1070-6631(00)00905-3]

I. INTRODUCTION

Stratified sheared turbulence occurs in many environmental and engineering flows. An improved understanding of the associated physics is essential for more accurate descriptions and prediction of these flows. An important aspect of turbulence is vortex stretching, that is, the interaction of vorticity ω and rate-of-strain S. This is a primary mechanism through which energy is transferred to the small scales. Physical experiments and numerical simulations have revealed various geometric properties and the presence of distinct small-scale structure in ω and S in unstratified turbulence.[1–12] For example, results from direct numerical simulations (DNS) of homogeneous turbulence show that moderate to intense ω tends to concentrate into sheetlike, tubelike, or filamentary structures.[3,4,8,10,13] Hairpin-shaped vortex structures are also observed in homogeneous shear flow[9] and may be particularly active sites for momentum and scalar transport.[14] In both isotropic and homogeneous sheared turbulence, a preferential alignment of ω with the intermediate principal strain eigenvector is observed,[1–6] particularly in regions of high magnitude ω and S. This can be explained in terms of the coupled dynamics of ω and S in the principal strain basis.[12] In this reference frame, vortex stretching and rotation of the principal axes of S are effectively distinguished. The latter mechanism includes both local and nonlocal effects and is associated with misaligned ω with respect to the principal axes. Locally-induced rotation of the S axes acts to orient misaligned ω towards the direction of either the intermediate or most compressive principal strain; the former associated with longer duration events (more probable state). Nonlocal effects, which include the influence of the proximate spatial structure, act through the pressure Hessian.[12] In homogeneous shear, the above dynamics are influenced by the imposed mean ω and S.[15] As a consequence, the spatial orientation of ω and the principal axes of S exhibit distinct directional preferences.

The structure of ω in stably stratified turbulent flows has also been investigated. Physical experiments[16] report a collapse of vortex structures and a predominance of horizontal ω. DNS of isotropic and homogeneous sheared turbulence with stratification report similar behavior.[14,17–19] In the case of homogeneous shear, both subcritical and supercritical Richardson numbers Ri are considered[14,17,18,20] (*subcritical* Ri flows exhibit growth of turbulent kinetic energy while *supercritical* Ri flows exhibit decay). With increasing stratification, ω exhibits an increased tendency to orient in the horizontal plane.[17] In subcritical flows, horseshoe, hairpin, and serpentine shaped structures are observed.[17,18] In supercritical flows, these structures are reportedly transformed into ring vortices or sheets and streaks. The ω in these flows is predominantly horizontal. The role of these structures in momentum and mass transport has also been investigated.[14,20] A simplified mathematical model for the low Froude number (high Ri) dynamics of a strongly stratified, weakly sheared

[a)]Phone: 858-534-5520; Fax: 858-534-7599; electronic mail: knomura@ucsd.edu

flow has been developed.[21] However, these exact solutions are laminar and therefore cannot describe the complete dynamics in a turbulent flow.

The previous studies of stratified turbulence considered the characteristics of ω. However, based on our studies of unstratified homogeneous turbulence,[12,15] it is evident that the *coupled* interaction of ω and S must be considered in order to fully understand the associated dynamics. With shear (mean velocity gradient) and stratification (mean density gradient), directional features in ω and S will influence the behavior of the scalar (density fluctuation) gradient, $\mathbf{G} \equiv \nabla \rho'$. Characteristics of the passive scalar gradient in homogeneous sheared turbulence have previously been considered.[2,5,22] In the presence of buoyancy (gravity effects), ρ is an active scalar, thus, $\mathbf{G}$ is an active vector which will influence the dynamics of ω and S. Previous studies of stably stratified homogeneous sheared turbulence which consider $\mathbf{G}$ are limited. The generation of temperature microfronts (regions of high temperature gradient) was considered for the case of subcritical stable stratification by examining the influence of pairs of hairpin vortices on the local temperature field.[14,23] Experimental measurements of the scalar gradient field have recently been obtained by Keller and Van Atta.[24] Their study shows characteristics of the scalar gradient for varying degrees of stratification.

As described below, the dynamics in stratified turbulence will involve a complex fully coupled interaction between ω, S, and $\mathbf{G}$. To our knowledge, this interaction has not been previously considered. We therefore investigate the coupled triadic interaction in order to provide a more complete description of the physics of stratified turbulence (note that here we use the term ''triadic interaction'' in the generic sense regarding the three quantities, ω, S, and $\mathbf{G}$, and not in reference to triadic interactions in wave number space). Results from DNS of stably stratified homogeneous shear flow are used in the analysis. To investigate the complex dynamics in detail, conditional sampling based on the invariants of the velocity gradient tensor is employed. This assists in distinguishing various mechanisms by considering the relative significance of rotation vs strain. We begin with a brief description of the dynamics under analysis. This is followed by presentation of the DNS results.

II. DYNAMIC INTERACTION

We consider an incompressible flow as described by the Navier–Stokes equations with the Boussinesq approximation for the fluid density ρ. In the presence of stratification and buoyancy, ρ is an active scalar and additional physical mechanisms are present. The behaviors of ω and S are influenced by the gradient of the density fluctuation, $\mathbf{G} \equiv \nabla \rho'$. Thus, ω, S, and $\mathbf{G}$ represent a coupled triadic system. The associated evolution equations are,

$$\frac{D\omega_i}{Dt} = \underbrace{S_{ik}\omega_k}_{\text{vortex stretching}} + \nu \frac{\partial^2 \omega_i}{\partial x_k \partial x_k} \underbrace{- \frac{g}{\rho_0}\epsilon_{ij3}G_j}_{\text{baroclinic torque}} \tag{2.1}$$

$$\frac{DS_{ij}}{Dt} = -S_{ik}S_{kj} \underbrace{- \tfrac{1}{4}(\omega_i\omega_j - \delta_{ij}\omega_k\omega_k)}_{\text{strain gen./rot.}} - \frac{1}{\rho}\frac{\partial^2 p}{\partial x_i \partial x_j} + \nu \frac{\partial^2 S_{ij}}{\partial x_k \partial x_k} \underbrace{- \frac{g}{2\rho_0}(G_j\delta_{i3} + G_i\delta_{j3})}_{\text{differential acceleration}} \tag{2.2}$$

$$\frac{DG_i}{Dt} = \underbrace{-S_{ik}G_k}_{\text{straining}} \underbrace{+ \tfrac{1}{2}\varepsilon_{ijk}\omega_j G_k}_{\text{rotation}} + D\frac{\partial^2 G_i}{\partial x_k \partial x_k} \tag{2.3}$$

Interaction between ω and S includes vortex stretching and strain generation and S axes rotation (2.1)–(2.2). The coupled dynamics of (2.1)–(2.2) in unstratified homogeneous turbulence are discussed in detail elsewhere.[12,15] Influence of ω and S on $\mathbf{G}$ is through amplification/reorientation by S and reorientation by ω (2.3). In the presence of buoyancy, there is direct feedback of $\mathbf{G}$ through baroclinic torque generation of ω (2.1) and through differential acceleration driven S (2.2). Thus, at a primary level, the triadic interaction can be considered in terms of the (direct) coupling of the following mechanisms; vortex stretching and strain generation and axes rotation (ω and S), gradient reorientation and baroclinic torque (ω and $\mathbf{G}$), and gradient amplification and differential acceleration (S and $\mathbf{G}$). The associated terms are underbraced in (2.1)–(2.3). At the secondary level, various repercussions of these coupled mechanisms will occur. The results presented will demonstrate the predominant interactions.

III. DIRECT NUMERICAL SIMULATIONS

DNS of homogeneous sheared turbulence with uniform stable stratification was performed for this study. Figure 1 shows profiles of the mean velocity $U(x_3)$ and density $\overline{\rho}(x_3)$. The gradients of the velocity and density are denoted by $S \equiv dU/dx_3$ and $\overline{G}_3 \equiv d\overline{\rho}/dx_3$, respectively. Relevant nondimensional parameters include the turbulent Reynolds number based on the Taylor microscale, $\mathrm{Re}_\lambda = \upsilon\lambda/\nu$, the Shear number, $\mathrm{Sh} = (\upsilon^2/\varepsilon)/(1/S)$, and the Schmidt number, $\mathrm{Sc} = \nu/D$. Here, υ is the rms velocity, ε is the energy dissipation rate, ν is the kinematic viscosity, and D is the mass diffusivity. The relative significance of stratification to mean shear effects is characterized by the Richardson number, $\mathrm{Ri} = N^2/S^2 = (-g\overline{G}_3/\rho_0)/S^2$, where N is the Brunt–Vaisala frequency, g is the acceleration of gravity (acting in the negative x_3 direction), and ρ_0 is a reference density. The governing equations describing the flow are the time-dependent continuity and Navier–Stokes equations with the Boussinesq approximation for the density. The computational domain is a finite cube containing 128^3 grid points.

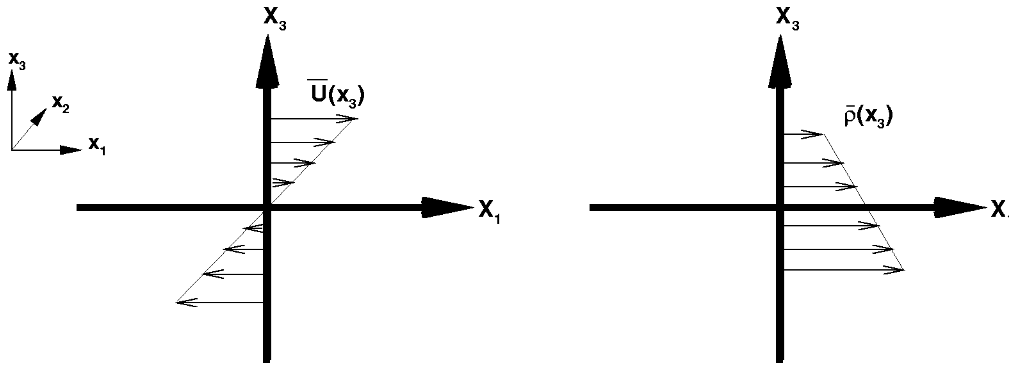

FIG. 1. Sketch of mean velocity and density profiles and coordinate system.

Periodic boundary conditions are employed in the x_1 (streamwise) and x_2 (spanwise) directions and shear-periodic conditions in the x_3 (mean gradient) direction.[25] The simulations are initialized with a fully developed isotropic turbulent velocity field and zero scalar fluctuations. The numerical solution employs a pseudospectral method.[25] The criterion,[26] $\eta k_{\max}>1$, was used to check for adequate grid resolution. In addition, the two-point velocity correlation $R_{11}(r_1)$ was evaluated as a suitable check for validity of periodic boundary conditions in the x_1 direction.[5]

Initial parameter values for the results presented here are $\mathrm{Re}_{\lambda_0}=20$ and $\mathrm{Sh}_0=3.2$. In addition, $\mathrm{Sc}=0.7$. Two cases are considered. In the case NB, buoyancy is absent $(g=0)$, thus $\mathrm{Ri}=0$. In the case HB, buoyancy effects are significant $(\mathrm{Ri}=1)$ and the flow is supercritically stratified. Note that in the results presented here, time is nondimensionalized by S. In the case of $\mathrm{Ri}=1$, since $N=S$, nondimensional time St is equivalent to Nt. From the computed flow field, various quantities associated with the velocity and scalar gradients are evaluated. The rate-of-strain tensor S, the vorticity vector ω, and the scalar gradient, $\mathbf{G}$, are computed from the spatial derivatives of the instantaneous velocity and scalar at each grid point and at each time. From S, the three principal eigenvalues $(\alpha \geqslant \beta \geqslant \gamma)$ and corresponding eigenvectors $(\boldsymbol{e}_\alpha, \boldsymbol{e}_\beta, \boldsymbol{e}_\gamma)$ are evaluated.

IV. RESULTS

A. General flow evolution

In the nonbuoyant NB flow, beyond a short period of decay due to the initial isotropic conditions,[27] the turbulent kinetic energy increases in time for the duration of the simulations. In contrast, the kinetic energy rapidly decays in the HB flow as expected for supercritical stratification. The energetics and evolution of large-scale quantities in stably stratified homogeneous shear flows have been investigated in previous DNS studies.[25,20,28,27] In this study, we focus our attention on small-scale quantities, i.e., gradients of the velocity and scalar. Note that, $r_\omega=\mathrm{Re}_{\lambda_0}/\mathrm{Sh}_0 \sim \langle \omega' \rangle / S = 6.25$, which indicates the significance of fluctuating vorticity to mean vorticity in the initial flow. Details of the unstratified homogeneous shear flow, including implications of r_ω, are discussed elsewhere.[15]

With regards to stratified turbulence, according to Gibson's fossil turbulence theory,[29–31] the evolution of a stably stratified homogeneous shear flow can be divided into three distinct phases. In the first phase, or *shear dominated flow*, the development of the small scales is controlled by the shear. During this time, the behavior of NB and HB are similar. The second phase is marked by the *onset of buoyancy control* where the small scales begin to feel the effects of buoyancy. At this time, characteristics of ω and S in NB and HB begin to differ. A quantitative criterion for the onset of this phase is the departure of the behavior of density from that of a passive scalar.[32] Examination of the time evolution of the rms components of $\mathbf{G}$ [Fig. 18(a)] shows that this departure occurs at approximately $\mathrm{St}=1$ (which corresponds to $\mathrm{Nt}=1$, or one Vaisala period). The third phase is that of *buoyancy dominated flow* (or complete *fossilization*) where buoyancy effects dominate the small scales. This occurs late in the evolution of the flow. Results which follow will be presented at times $\mathrm{St}=0.5, 2$, and 6. The latest time, $\mathrm{St}=6$, corresponds to approximately the end of the second phase. We thus consider the behavior of the small scales during a period in which turbulence remains active and shear and buoyancy effects may strongly interact.

B. Conditional sampling

In the results to be presented, conditional statistics associated with distinct high-amplitude events are considered. These provide detailed information concerning the structure and dynamics of ω and S. Recall that the *local* flow can be characterized in terms of the invariants of the velocity gradient tensor. For an incompressible flow, the three invariants can be expressed as,[12]

$$\mathrm{I}=-(\alpha+\beta+\gamma)=0, \tag{4.1}$$

$$\mathrm{II}=\tfrac{1}{2}(\omega^2/2-\mathsf{S}^2), \tag{4.2}$$

$$\mathrm{III}=-\alpha\beta\gamma-\tfrac{1}{4}(\alpha\omega_\alpha^2+\beta\omega_\beta^2+\gamma\omega_\gamma^2), \tag{4.3}$$

where α, β, γ, are the eigenvalues of S. Thus, II indicates the relative significance of ω and S while III indicates the structure of S and the nature of interaction of ω and S. Figure 2 shows the joint probability of II and III for the NB and HB flow fields. The values of II and III are normalized by $\langle \omega^2 \rangle$ and $\langle \omega^2 \rangle^{3/2}$, respectively, for the given time. The

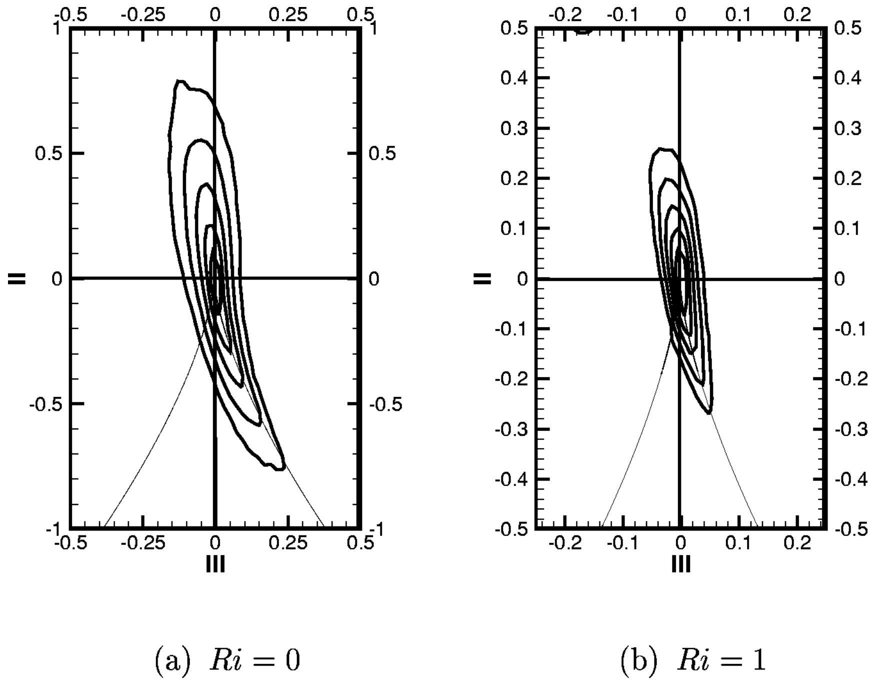

FIG. 2. Joint probability distribution of normalized invariants II and III at St=6: (a) Ri=0 (NB), (b) Ri=1 (HB). Contour values correspond to $\log(10^6 P+1)$, where P is the probability.

zero discriminant ($D=0$) curve which separates complex and real eigenvalues is included in these plots. In both cases, the highest probability occurs at the origin (recall for homogeneous flows,[33] $\langle \mathrm{II}\rangle=0$ and $\langle \mathrm{III}\rangle=0$). In addition, high-amplitude II exhibits a preference for the upper left ($\mathrm{II}>0, \mathrm{III}<0$: QII) and lower right ($\mathrm{II}<0, \mathrm{III}>0$: QIV) quadrants as is observed in other turbulent flows.[12,34] We therefore consider conditional samples associated with these topologies. Each conditional sample will be referred to by the particular quadrant of the II–III plane, i.e., sample QII consists of high-amplitude rotation-dominated regions ($\mathrm{II}>0, \mathrm{III}<0$) while sample QIV consists of high-amplitude strain-dominated regions ($\mathrm{II}<0, \mathrm{III}>0$). In addition, we consider a sample Q0 which consists of high-amplitude events with comparable rotation and strain ($\mathrm{II}\approx 0$). The QII and QIV samples are limited to high-amplitude regions by $\sqrt{\mathrm{II}^2+\mathrm{III}^2}\geqslant r_{\mathrm{th}}$, where r_{th} is a selected threshold. A threshold on Q0 is imposed by considering $\omega^2 \geqslant r_{\mathrm{th}}\langle\omega^2\rangle$. In each sample, the threshold level r_{th} is adjusted so that the sample size is approximately 5% of the total grid points. In general, we expect that these high-amplitude events will more clearly display and emphasize the associated characteristic behavior for the sampled region. Results from our previous analysis of homogeneous shear[15] demonstrate that these high amplitude conditional samples capture the basic features observed in the total flow.

C. Spatial structure

As discussed in the Introduction, high-amplitude ω^2 regions in homogeneous turbulence are associated with both tubelike and sheetlike spatial structures. These are effectively distinguished by considering the second invariant II (Refs. 10 and 15) (the significance of III with regards to structures has also been considered[12]). With stratification and buoyancy, the nature of these structures changes as Ri increases. Figure 3 shows isoscalar surfaces of high-amplitude $\mathrm{II}>0$ (rotation-dominated) for both the NB and HB flows. The tubelike structure characteristic of these regions is clearly evidenced in the flow without buoyancy [NB, Figs. 3(a) and 3(b)]. Due to the effects of mean shear, these structures exhibit distinct spatial orientation. In the side view [Fig. 3(b)], the tubes are seen to orient at approximately 20°–35° upwards from the horizontal while the top view [Fig. 3(a)] indicates a developing inclination[15] towards the spanwise (x_2) direction. In general, tubelike structures persist in high-amplitude $\mathrm{II}>0$ regions in flows with buoyancy for low Ri. As Ri increases and the flow becomes supercritical [HB, Figs. 3(c) and 3(d)], the structures tend to flatten and collapse towards the horizontal plane of the flow. Figure 4 shows structures associated with regions of high-amplitude and comparable rotation and strain (Q0). In the NB flow [Figs. 4(a) and 4(b)], wavy, sheetlike structures are observed (the wavy attribute refers to the large undulations of the structures rather than the small ripples which are an artifact of the graphics). These structures have significant spanwise extent [Fig. 4(a)] and are also inclined from the horizontal [Fig. 4(b)]. In the HB flow [Figs. 4(c) and 4(d)], the spanwise extent of the structures is considerably reduced. The wavy feature is eliminated and the structures become distinctly planar as seen in the side view [Fig. 4(d)]. In general, high-amplitude strain-dominated ($\mathrm{II}<0$) regions in shear flow (not shown) are not as geometrically distinct as rotation-dominated or Q0 regions and tend to be more discontinuous. The associated structures also tend to incline from the horizontal, the inclination being significantly less in the HB flow.

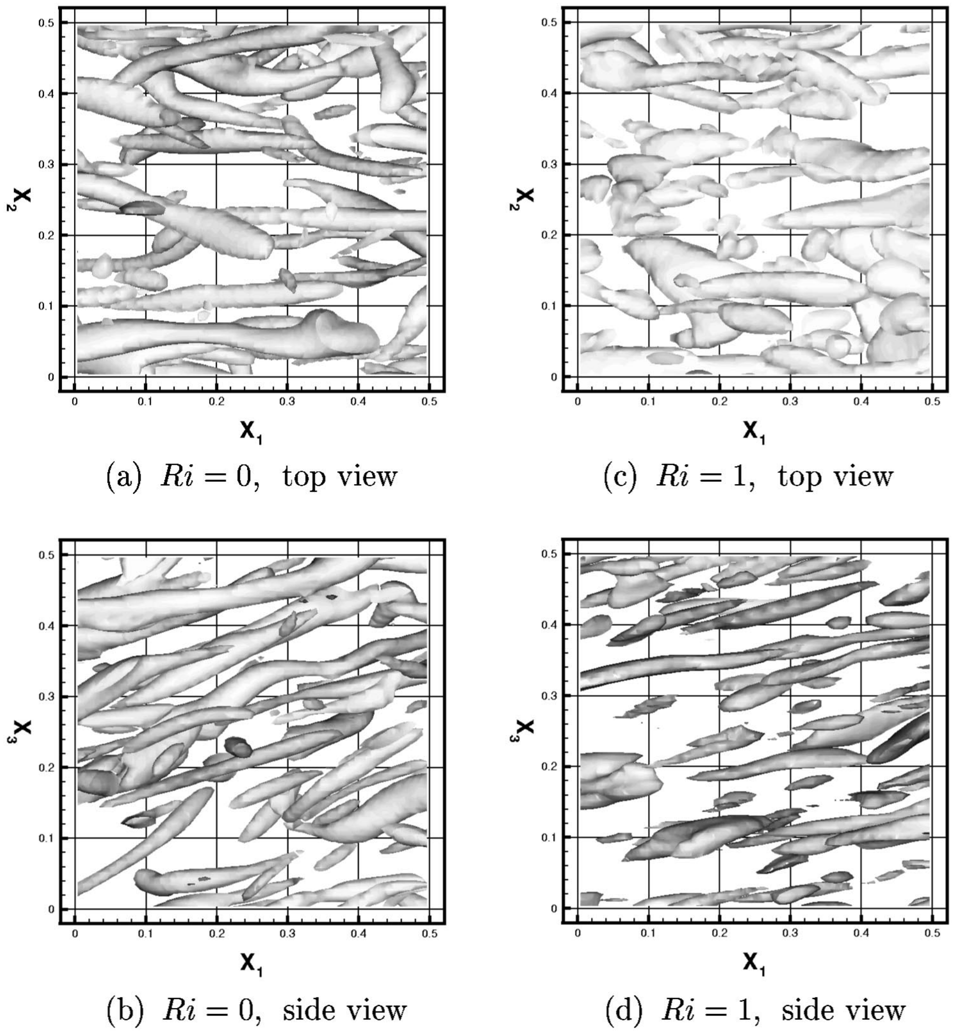

FIG. 3. Three-dimensional visualizations (64^3 subdomain of computational grid) of high-amplitude rotation-dominated (II>0) regions in homogeneous shear flow at time St=6: (a) Ri=0, top view, (b) Ri=0, side view, (c) Ri=1, top view, (d) Ri=1, side view. Isoscalar surfaces correspond to threshold magnitude of $\mathrm{II}=0.35\langle\omega^2\rangle$ for Ri=0 and $\mathrm{II}=0.1\langle\omega^2\rangle$ for Ri=1.

D. Interaction of $\boldsymbol{\omega}$ and S

We now consider the spatial orientation of ω and the principal eigenvectors of S. In general, the orientation of a vector $\mathbf{V}$ in Cartesian coordinate space can be defined by the angle pair $(\theta_{\mathrm{pitch}},\theta_{\mathrm{yaw}})$ where θ_{pitch} is the angle of $\mathbf{V}$ from its projection on the x_1-x_2 (horizontal) plane and θ_{yaw} is the angle of the projection from the positive x_2-axis (see Fig. 5). Since $(0°,0°)$ is the orientation of the vorticity associated with the mean shear $\overline{\omega}$, the angle pair defines the orientation of a vector with respect to this reference direction. A joint probability distribution (jpd) of the angle pair may then be used to determine the most probable orientation for a given sample. Due to an inherent bias which exists in the defined geometry,[15] $\sin\theta_{\mathrm{pitch}}$ rather than θ_{pitch} is used in the angle pair jpd to correctly indicate the probable $(\theta_{\mathrm{pitch}},\theta_{\mathrm{yaw}})$.

Figure 6 shows the $(\theta_{\mathrm{pitch}},\theta_{\mathrm{yaw}})$ jpds for fluctuating vorticity $\omega'=\omega-\overline{\omega}$ in the NB and HB flows at St=6 (onset of buoyancy control in HB). Note that in both flows, $|\theta_{\mathrm{pitch}}|<45°$ and $|\theta_{\mathrm{yaw}}|>90°$ prevail. The distributions also tend to follow an underlying reverse ''S'' shape. The significance of these attributes will later be explained. In the HB flow [Fig. 6(b)], the jpd shifts towards the $\theta_{\mathrm{pitch}}=0$ axis which corresponds to the horizontal plane. This is in agreement with the previously reported predominance of horizontal ω in stratified flows.[14,17–20] Figure 7 shows the orientation of ω' for each of the conditional samples. The directional features observed in the overall flows (Fig. 6) are now associated with their contributing regions. The characteristics of each of the samples are discussed below.

We first consider the high amplitude rotation-dominated QII regions [Figs. 7(a) and 7(d), NB: $r_{\mathrm{th}}=0.35$, HB: $r_{\mathrm{th}}=0.10$]. At very early times (St<1, not shown), both flows exhibit similar features. The peaks in the jpds occur near $(\theta_{\mathrm{pitch}},\theta_{\mathrm{yaw}})=(\pm 45°,\pm 90°)$ indicating initial amplification in the direction of the mean extensional strain, $\overline{\boldsymbol{e}_\alpha}$. As the NB flow develops, $|\theta_{\mathrm{pitch}}|$ decreases while $|\theta_{\mathrm{yaw}}|$ increases. At St=2 (not shown), the most probable orientation corresponds to $(\pm 35°,\pm 105°)$. As the flow further develops, θ_{pitch} stabilizes at about $\pm 20°$ while θ_{yaw} increases and then maintains at approximately $\pm 120°$ [Fig. 7(a)]. In the buoyant HB flow [St=6, Fig. 7(d)], a significant reduction in θ_{pitch} values along with the development of spanwise ω' $(0°,0°)$ is observed. The distribution essentially develops towards the $\theta_{\mathrm{pitch}}=0°$ axis. The corresponding orientation of instantaneous ω in both flows is generally consistent with the behavior of the corresponding structures [Figs. 3(c) and 3(d)].

Figures 7(b), 7(e) show results for the Q0 (comparable

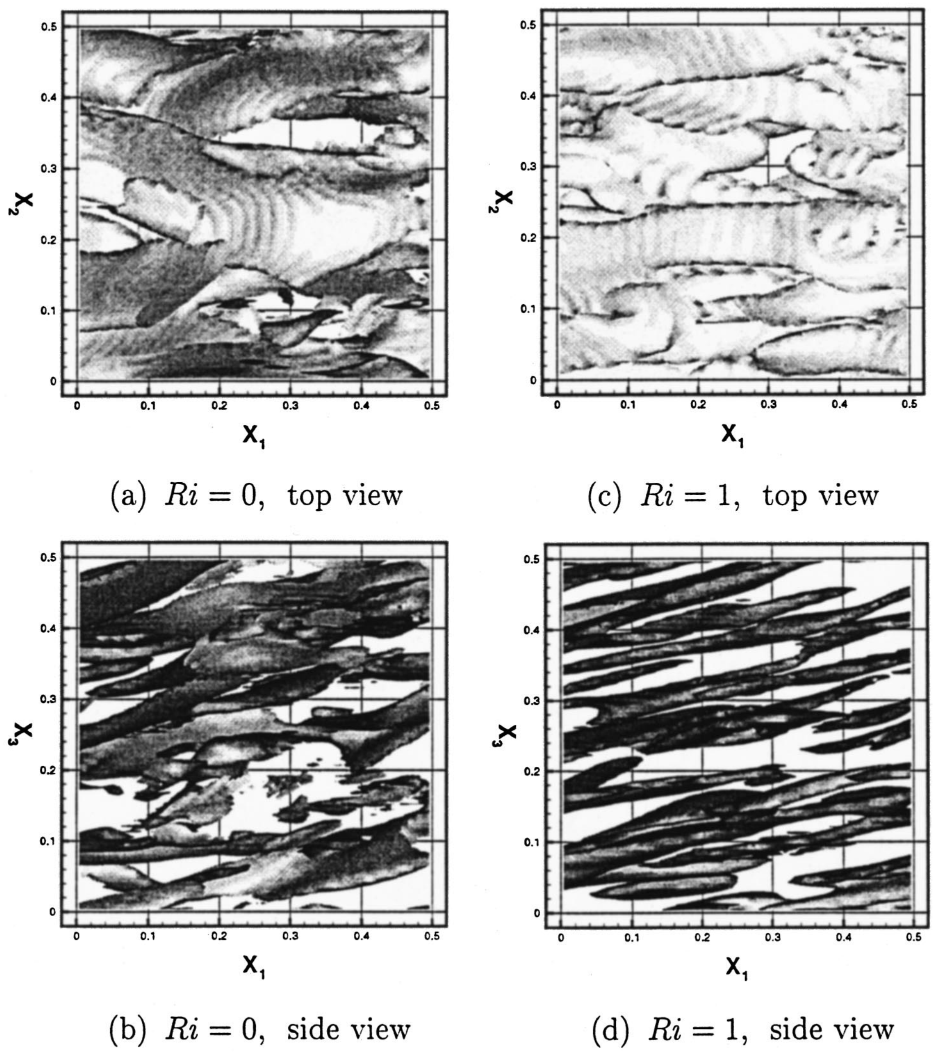

FIG. 4. Three-dimensional visualizations (64^3 subdomain of computational grid) of high-amplitude, comparable rotation and strain ($\mathrm{II}\sim 0$) regions in homogeneous shear flow at time St=6: (a) Ri=0, top view, (b) Ri=0, side view, (c) Ri=1, top view, (d) Ri=1, side view. Isoscalar surfaces are conditioned by $\omega > 2\langle\omega^2\rangle$.

rotation and strain) regions. In the NB flow at very early times, the jpds again indicate initial amplification along $\overline{\boldsymbol{e}_\alpha}$. In time [Fig. 7(b)], significant positive spanwise ω' ($\theta_{\rm yaw}=0°$) develops. This is accompanied by a range of values of $\theta_{\rm pitch}$ which may be associated with the wavy feature exhibited by the isosurfaces of these regions [Figs. 4(a), 4(b)]. In the HB flow at an earlier time, there is greater variation in $\theta_{\rm pitch}$ and $\theta_{\rm yaw}$ although positive spanwise ω' dominates. As the flow develops, $\theta_{\rm pitch}$ values are reduced and ω' is limited primarily to the positive spanwise direction [Fig. 7(e)]. Recall that in the corresponding isosurfaces [Figs. 4(c), 4(d)], the wavy feature is eliminated and the structures tend to be rather planar.

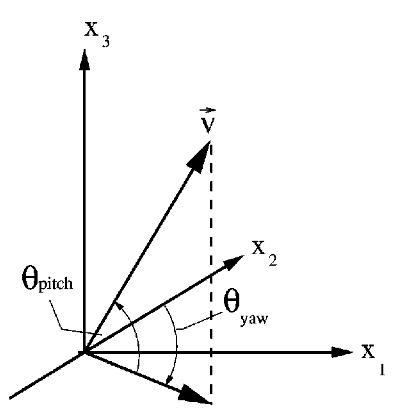

FIG. 5. Definition of the angles of orientation ($\theta_{\rm pitch}$, $\theta_{\rm yaw}$) of a vector in 3D Cartesian coordinates.

The orientation of ω' in the strain-dominated QIV sample is shown in Figs. 7(c), 7(f). In the NB flow at an earlier time (St=2, not shown), the jpd follows a reverse ''S''-shaped curve with peaks corresponding to approximately $(\pm 30°, \pm 120°)$. As in Q0, in time [Fig. 7(c)], significant positive spanwise ω' develops which is accompanied by a range of $\theta_{\rm pitch}$. In the HB flow [Fig. 7(f)], the prevalence of positive spanwise ω' is established earlier in time. The reverse ''S''-shape is also evident in these distributions.

Before examining the spatial orientation of the S eigenvectors, we consider the interaction of ω and S in homogeneous shear flow without buoyancy effects. This is discussed in detail elsewhere.[15] Here, we summarize what is needed to understand the presented results. The associated dynamics are best described by considering Eqs. (2.1)–(2.2) in the principal strain basis.[12,15] In addition to direct interaction

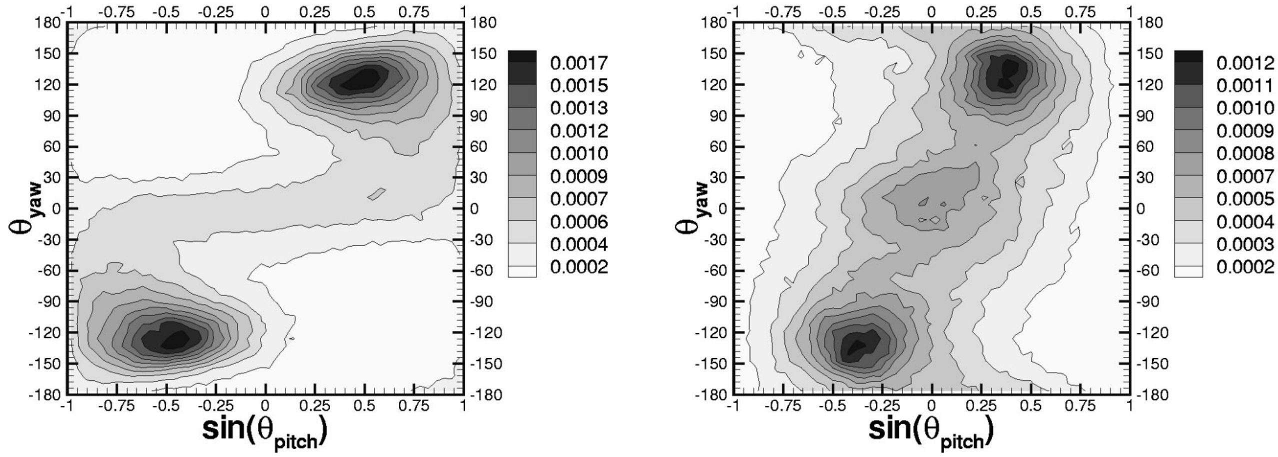

(a) $Ri=0$ (b) $Ri=1$

FIG. 6. Joint probability distributions indicating the angles of orientation ($\theta_{\mathrm{pitch}}, \theta_{\mathrm{yaw}}$) of ω' for total flow (St=6): (a) Ri=0, (b) Ri=1.

through vortex stretching, ω and S interact through locally- and nonlocally-induced rotation of the principal axes and through generation of strain. The induced rotations are associated with misaligned ω with respect to S. As indicated by restricted Euler equations,[35,12] locally-induced rotation of the principal axes acts to orient ω towards the direction of either the intermediate or most compressive principal strain.

In the early development of homogeneous shear flow,[15] amplification of ω' in the direction of the extensional strain of the mean shear, $\overline{\boldsymbol{e}}_\alpha$, prevails. A schematic of the geometry is given in Figs. 8(a), 8(b). The presence of mean vorticity $\overline{\omega}$ establishes a *predominant misalignment* of ω with respect to the principal axes of S which results in a locally-induced rotation of the S axes[15] [Fig. 8(b)]. If the eigenvectors of $\overline{\mathrm{S}}$ initially coincide with those of the mean shear, i.e., $\overline{\boldsymbol{e}}_\alpha$, $\overline{\boldsymbol{e}}_\beta$ ($\overline{\beta}=0$), and $\overline{\boldsymbol{e}}_\gamma$, the induced rotation ($D\boldsymbol{e}_\alpha/Dt\cdot\boldsymbol{e}_\beta$) will reorient $\boldsymbol{e}_\alpha$ and $\boldsymbol{e}_\beta$ in the plane comprised of $\overline{\boldsymbol{e}}_\alpha$ and $\overline{\boldsymbol{e}}_\beta$. This plane corresponds to a reverse ''S''-shaped curve in the ($\theta_{\mathrm{pitch}}, \theta_{\mathrm{yaw}}$) plot [Fig. 8(c)]. We will refer to this plane as the S^+-plane. The sense of rotation is such that $\boldsymbol{e}_\beta$ is directed towards ω (restricted Euler dynamics). Further amplification of ω' will occur along the reoriented principal axes. If this mechanism is significant and persistent, we expect ω' (and instantaneous ω) to orient in the S^+-plane. The distributions in Figs. 6 and 7 show some tendency to follow the S^+-plane curve consistent with the described dynamics. In general, the presence of ω' in other directions (isotropic initial conditions) will cause the rotation of the principal axes to vary. In particular, misaligned ω in the $\overline{\boldsymbol{e}}_\beta-\overline{\boldsymbol{e}}_\gamma$ plane induces rotation of $\boldsymbol{e}_\gamma$ and $\boldsymbol{e}_\beta$ about the axis of $\boldsymbol{e}_\alpha$. The sense of rotation in this case is such that $\boldsymbol{e}_\gamma$ is directed towards ω. The $\overline{\boldsymbol{e}}_\beta-\overline{\boldsymbol{e}}_\gamma$ or S^--plane corresponds to a *forward* S-shaped curve in the two angle plot.[15] The simultaneous reorientation of the three principal axes may result in rather complex orientations in S and ω.

Evidence of *S-plane* dynamics is apparent in the orientation of the eigenvectors of S (Figs. 9–12). In the NB flow [total flow, Figs. 9(a)–9(c)], the distributions for $\boldsymbol{e}_\alpha$ and $\boldsymbol{e}_\beta$ generally follow the S^+-plane curve while that of $\boldsymbol{e}_\gamma$ follows the S^--plane curve. Similar behavior is observed in the QII and Q0 samples [Figs. 10(a)–10(c), Figs. 11(a)–11(c)], while in the QIV sample [Figs. 12(d)–12(f)], $\boldsymbol{e}_\alpha$ and $\boldsymbol{e}_\beta$ have essentially switched locations by the time shown. As indicated by the strain basis equations,[12,15] the rates of locally-induced rotation are proportional to the vorticity components, e.g.,

$$\frac{D\boldsymbol{e}_\alpha}{Dt}\cdot\boldsymbol{e}_\beta=-\frac{1}{\alpha-\beta}\Big(\underbrace{\tfrac{1}{4}\omega_\alpha\omega_\beta}_{\text{locally-induced}}+\tilde{\Pi}_{\alpha,\beta}\Big). \tag{4.4}$$

We may then expect these effects to be particularly significant in QII regions of the flow. However, the tendency for β to approach α in high S^2 regions effectively enhances[12] the rate of rotation of $\boldsymbol{e}_\alpha-\boldsymbol{e}_\beta$ ($D\boldsymbol{e}_\alpha/Dt\cdot\boldsymbol{e}_\beta$) by increasing the prefactor in Eq. (4.4). This explains the observed behavior of QIV in NB [Figs. 12(d), 12(e)]. In regions with significant strain, the induced rotation and associated reorientation of $\boldsymbol{e}_\alpha$ towards the spanwise direction is accompanied by amplification of spanwise ω as evidenced in Figs. 7(b), 7(c). In general, the directional features of the S axes in the total flow [Figs. 9(a)–9(c)] are captured by the Q0 and QIV samples [Figs. 11(a)–11(c), 12(a)–12(c)].[15] With regards to nonlocal effects,[12,15] recall that high-amplitude rotation-dominated regions are associated with tubelike spatial structure [Figs. 3(a), 3(b)]. This generates a counteracting nonlocally-induced rotation of the principal axes in QII which acts through $\tilde{\Pi}_{\alpha,\beta}$ in Eq. (4.4). In QIV, the counteracting nature of $\tilde{\Pi}$ is not present and locally-induced rotation readily occurs in these regions.

We now examine the orientation of the S eigenvectors in HB where buoyancy effects are present. Figures 9(d)–9(f) shows the jpds for the total flow at time St=2 (onset of buoyancy control). These results suggest a reduction in locally-induced rotation of the S axes as compared with NB

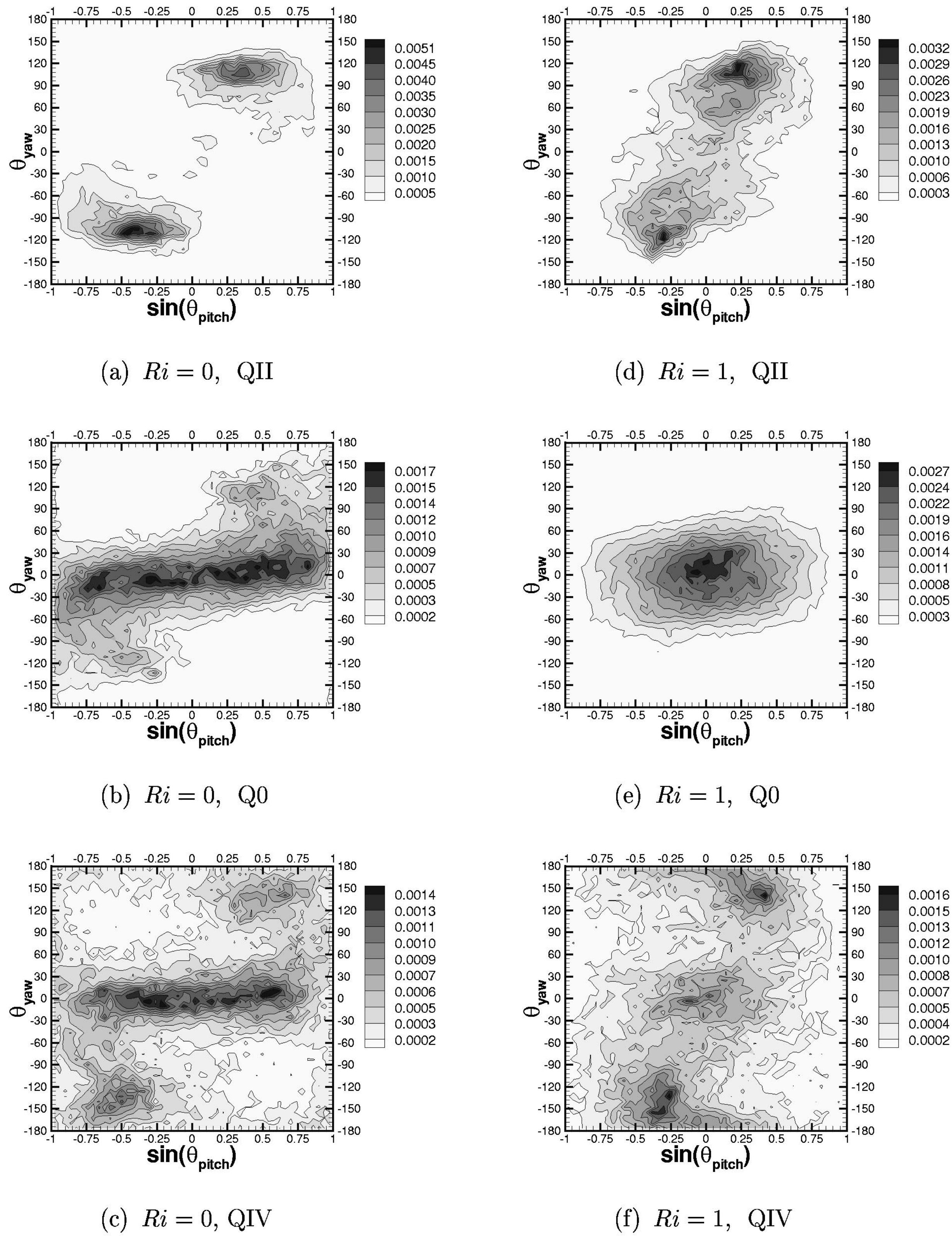

FIG. 7. Joint probability distributions indicating the angles of orientation ($\theta_{pitch}, \theta_{yaw}$) of ω' for QII, Q0, and QIV conditional samples: (a)–(c) Ri=0, (d)–(f) Ri=1 (St=6).

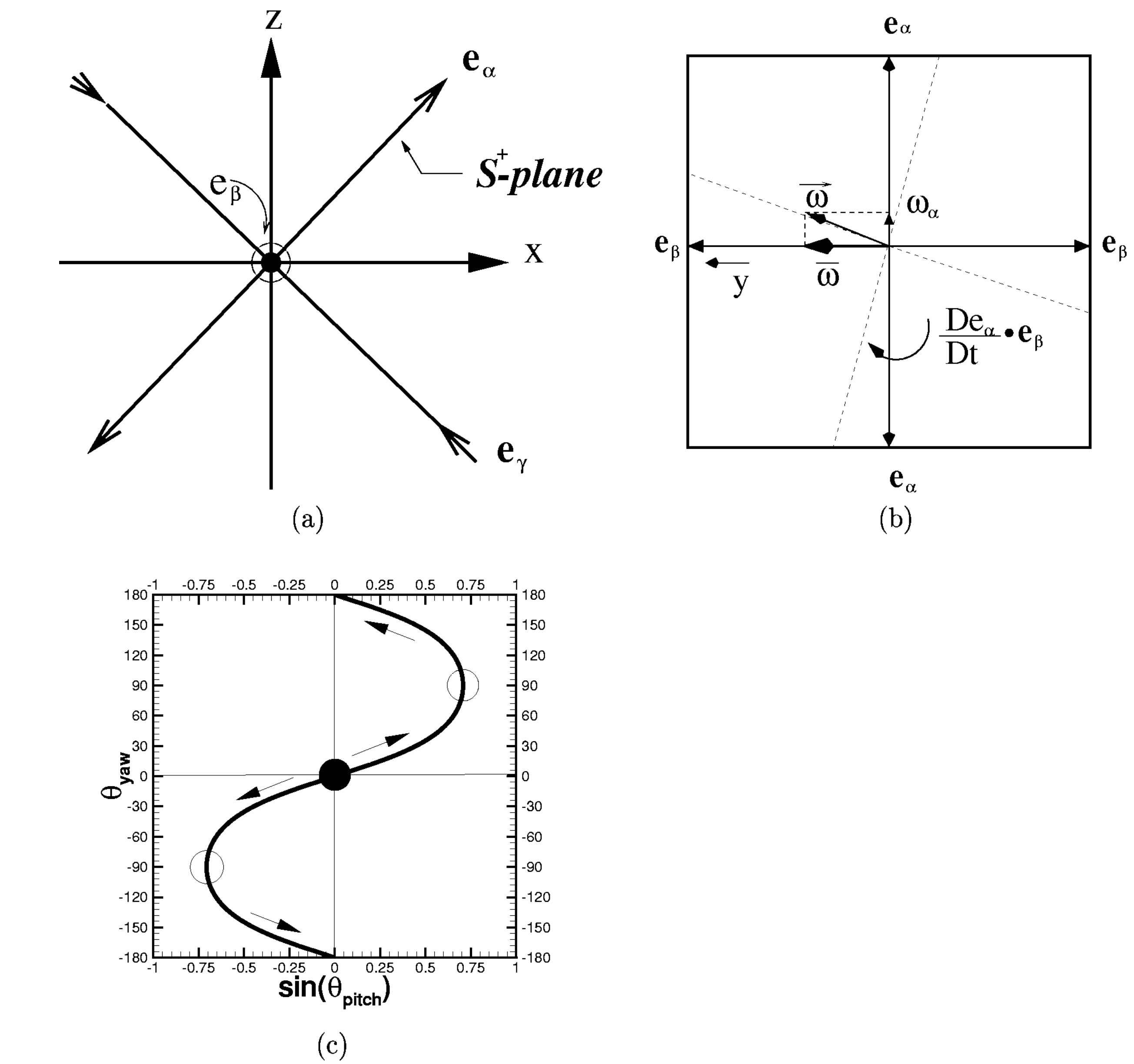

FIG. 8. *S*-plane structure and dynamics; (a) coordinate system with principal strain eigenvector directions corresponding to mean shear, (b) diagram of S^+-plane indicating ω induced (clockwise) rotation of the principal axes, (c) S^+-plane curve on $\sin(\theta_{\rm pitch})$ vs $\theta_{\rm yaw}$ plot. Note ○ indicates orientation of $\overline{\boldsymbol{e}_\alpha}$, ● indicates orientation of $\overline{\boldsymbol{e}_\beta}$, and arrows indicate trajectories of principal axes. Upper right quadrant associated with the *clockwise* rotation of the principal axes as indicated in (b) while lower left quadrant associated with a *counterclockwise* rotation occurring in S^+-plane.

[Figs. 9(a)–9(c)]. The distributions in the QII sample [Figs. 10(d)–10(f)] generally resemble those of the total flow. We note that $\boldsymbol{e}_\gamma$ [Fig. 10(f)] exhibits higher values of $\theta_{\rm pitch}$ than that corresponding to NB [Fig. 10(c)]. In the Q0 sample [Figs. 11(d)–11(f)], although there is some indication of *S*-plane dynamics occurring, the orientation of the eigenvectors does not show significant variation, i.e., the distributions are rather confined. In QIV [Figs. 12(d)–12(f)], the distributions of $\boldsymbol{e}_\alpha$ and $\boldsymbol{e}_\beta$ tend to follow the S^+-plane curve, however, $\boldsymbol{e}_\alpha$ and $\boldsymbol{e}_\beta$ do not attain the orientations exhibited by QIV in NB [Figs. 12(b), 12(c)]. As will be discussed, locally-induced rotation of the strain axes is impeded in this flow. At later times ($\mathrm{St}=6$, not shown), the orientation of the strain axes in the total flow (and conditional samples) tends toward that of the imposed mean shear as the turbulent fluctuations are damped out by buoyancy.

In general, the mechanisms associated with the interaction of ω and S in NB remain active in HB for the considered time interval. Differences in behavior of HB are due to the additional mechanisms associated with the active scalar gradient. In order to understand these dynamics, we will first look at the case of a passive scalar gradient and the associated (one-way) interaction with the flow field.

E. Passive scalar gradient dynamics

We now consider the behavior of the scalar gradient **G** in shear flow without buoyancy (NB). In this case, ρ is a

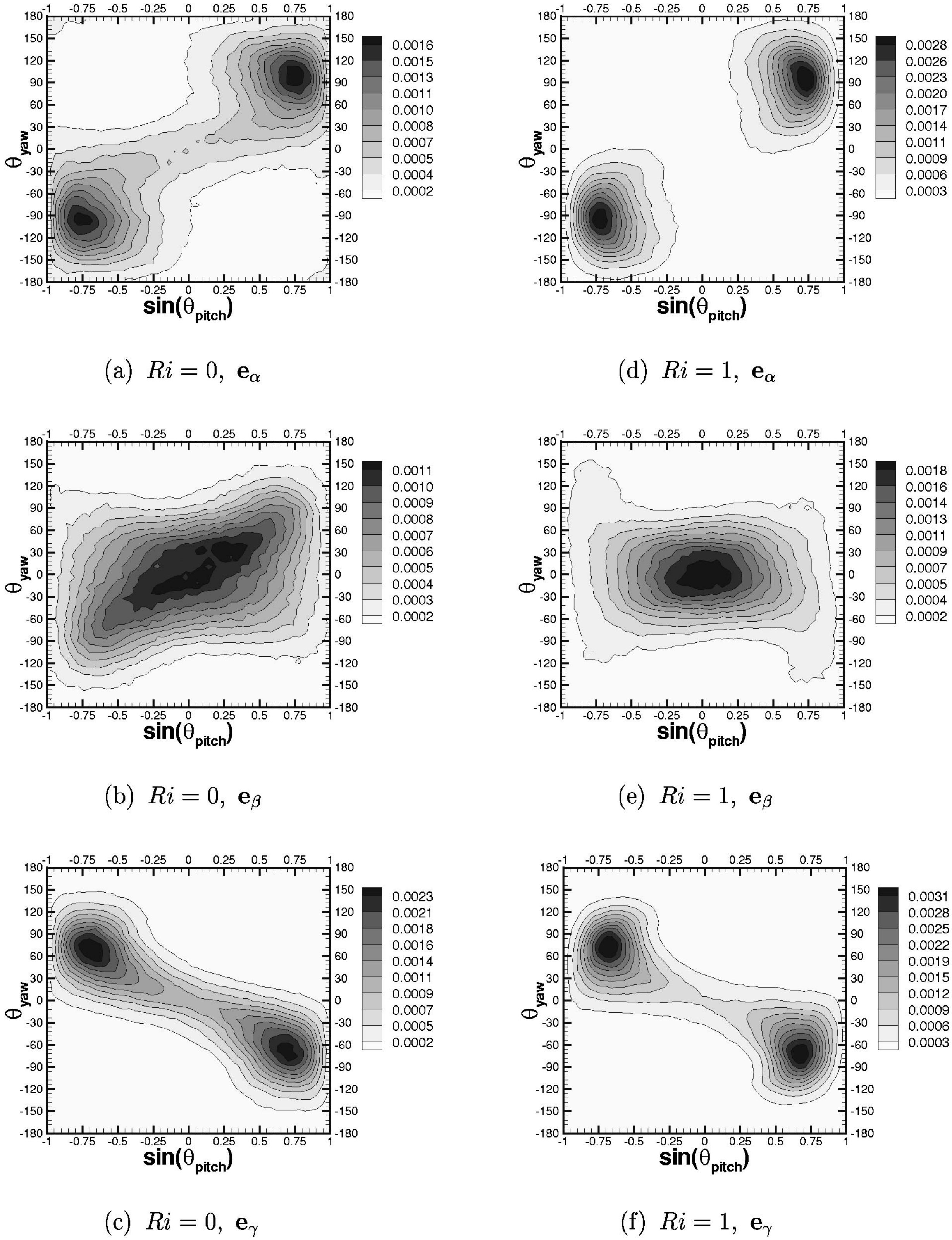

FIG. 9. Joint probability distributions indicating the angles of orientation $(\theta_{\text{pitch}}, \theta_{\text{yaw}})$ of S eigenvectors $\boldsymbol{e}_\alpha$, $\boldsymbol{e}_\beta$, $\boldsymbol{e}_\gamma$, for total flow: (a)–(c) Ri=0, (d)–(f) Ri=1 (St=2).

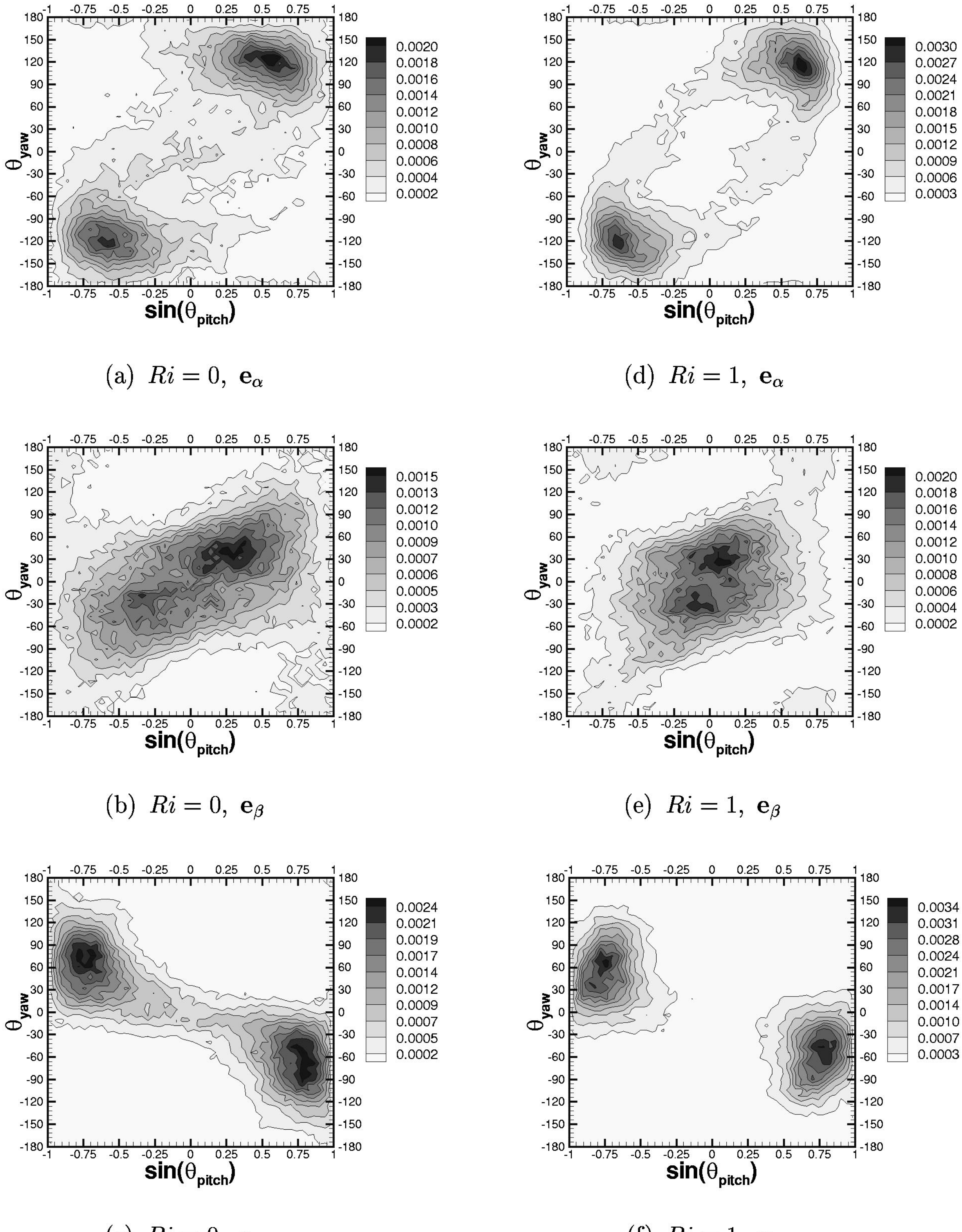

(a) $Ri = 0,\ \mathbf{e}_\alpha$ (d) $Ri = 1,\ \mathbf{e}_\alpha$

(b) $Ri = 0,\ \mathbf{e}_\beta$ (e) $Ri = 1,\ \mathbf{e}_\beta$

(c) $Ri = 0,\ \mathbf{e}_\gamma$ (f) $Ri = 1,\ \mathbf{e}_\gamma$

FIG. 10. Joint probability distributions indicating the angles of orientation ($\theta_{\rm pitch}, \theta_{\rm yaw}$) of S eigenvectors $\boldsymbol{e}_\alpha$, $\boldsymbol{e}_\beta$, $\boldsymbol{e}_\gamma$, for QII conditional sample: (a)–(c) Ri=0, (d)–(f) Ri=1 (St=2).

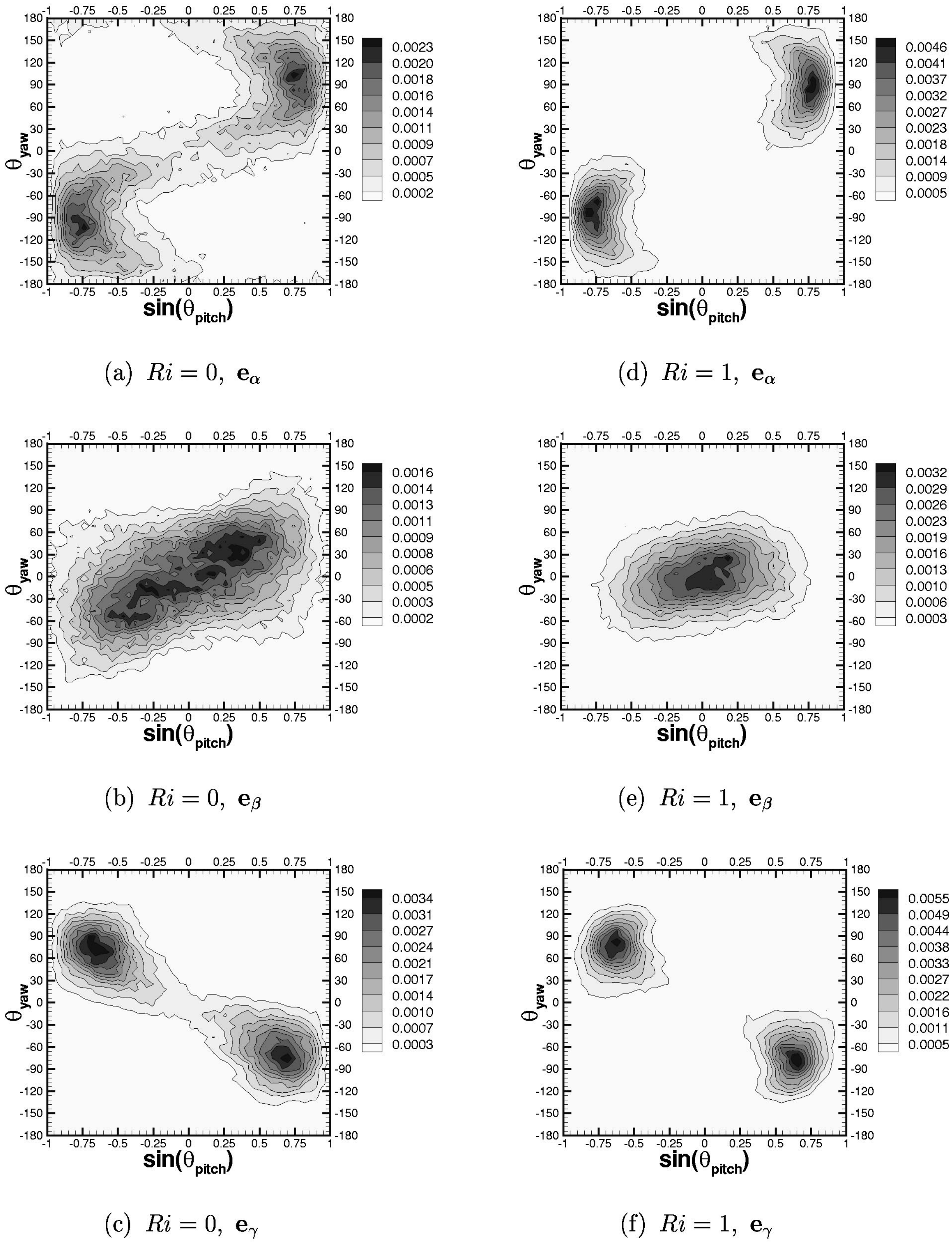

FIG. 11. Joint probability distributions indicating the angles of orientation ($\theta_{\mathrm{pitch}}, \theta_{\mathrm{yaw}}$) of S eigenvectors $\boldsymbol{e}_\alpha$, $\boldsymbol{e}_\beta$, $\boldsymbol{e}_\gamma$, for Q0 conditional sample: (a)–(c) Ri=0, (d)–(f) Ri=1 (St=2).

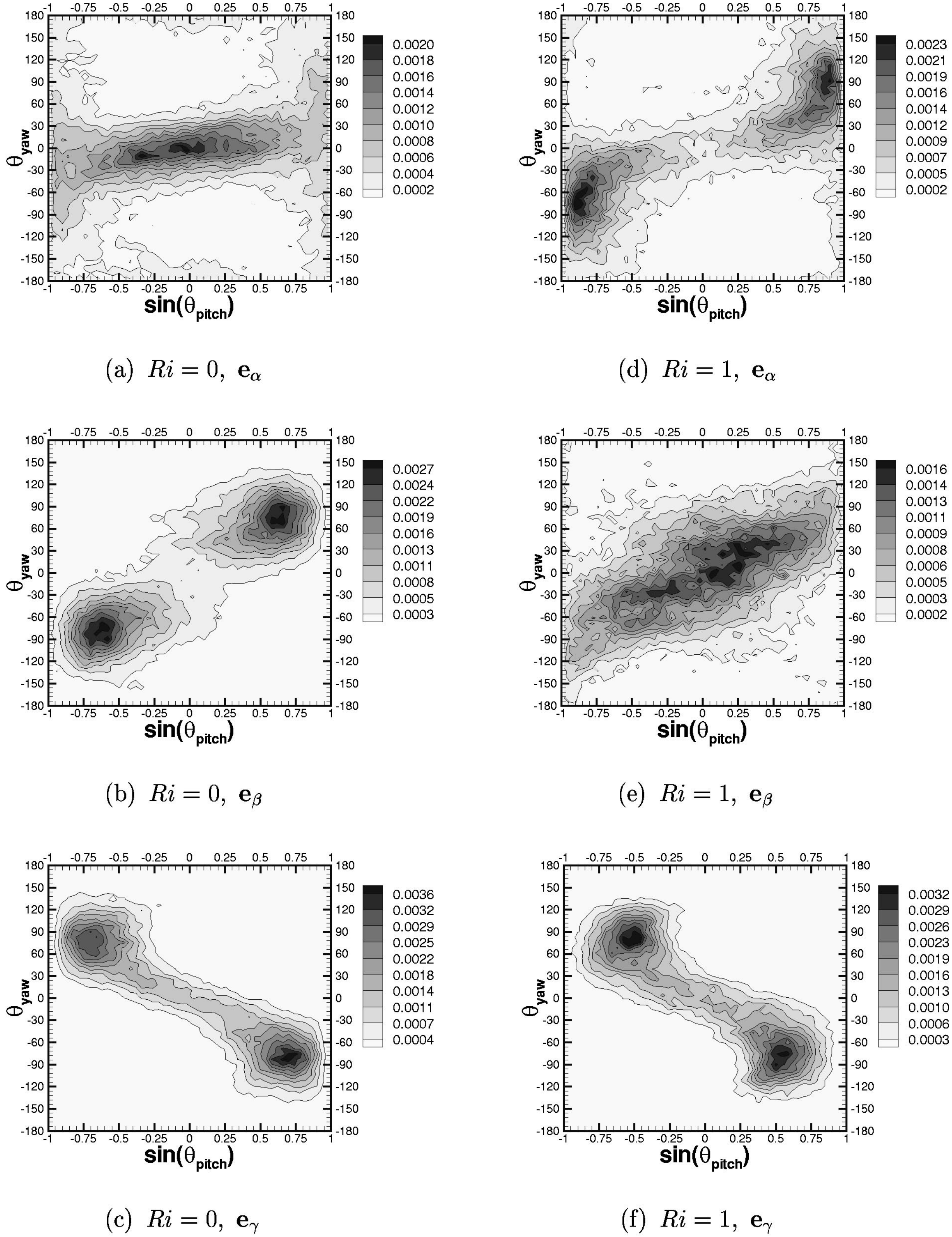

FIG. 12. Joint probability distributions indicating the angles of orientation ($\theta_{\mathrm{pitch}}, \theta_{\mathrm{yaw}}$) of S eigenvectors $\boldsymbol{e}_\alpha$, $\boldsymbol{e}_\beta$, $\boldsymbol{e}_\gamma$, for QIV conditional sample: (a)–(c) Ri=0, (d)–(f) Ri=1 (St=2).

passive scalar and the dynamics of **G** are one-way coupled to ω and S [Eq. (2.3)]. A decomposition of the field variables into their mean and fluctuating components is applied to Eq. (2.3) resulting in the evolution equation for fluctuating G. The component equations are written here without the diffusion terms and, hereafter, the primes indicating fluctuating components are dropped,

$$\frac{DG_1}{Dt} = -(S_{11}G_1 + S_{12}G_2 + \underbrace{S_{13}G_3}_{GS1} + \underbrace{S_{13}\bar{G}_3}_{GS2}) + \tfrac{1}{2}(\underbrace{\omega_2\bar{G}_3}_{GR1} + \underbrace{\omega_2 G_3}_{GR2} - \omega_3 G_2) \qquad (4.5)$$

$$\frac{DG_2}{Dt} = -(S_{21}G_1 + S_{22}G_2 + S_{23}G_3 + S_{23}\bar{G}_3) + \tfrac{1}{2}(\underbrace{\omega_3 G_1}_{GR3} - \underbrace{\omega_1 G_3}_{GR4} - \underbrace{\omega_1\bar{G}_3}_{GR5}) \qquad (4.6)$$

$$\frac{DG_3}{Dt} = -(S_{31}G_1 + S_{32}G_2 + \underbrace{S_{33}G_3}_{GS3} + \bar{S}_{13}G_1 + \underbrace{S_{33}\bar{G}_3}_{GS4}) + \tfrac{1}{2}(\underbrace{\omega_1 G_2}_{GR6} - \underbrace{\omega_2 G_1}_{GR7} - \bar{\omega}_2 G_1) \qquad (4.7)$$

The evolution and significance of the individual terms have been evaluated for each of the conditional samples and total flow (not shown). The terms corresponding to the observed dominant mechanisms are underbraced. The associated physics are described below.

As will be discussed, preferential orientation in **G** is established primarily by the prevailing fluctuating ω. We recall the results of the previous section which characterize ω in each of the conditional samples. Early in the development of the flow, amplification of fluctuating ω by the mean extensional strain promotes streamwise and vertical components, i.e., $\pm\omega_1$ and $\pm\omega_3$, respectively. As a consequence of the *S*-plane dynamics, streamwise $\pm\omega_1$ and negative spanwise vorticity $-\omega_2$ ($|\theta_{\text{yaw}}|>90°$) are promoted while $\pm\omega_3$ is reduced. These components are maintained for some time in QII. In Q0 and QIV, *S*-plane dynamics also occur and, in time, lead to the development of $+\omega_2$ which is accompanied by $\pm\omega_3$. Note, due to the presence of mean shear and the imposed sampling conditions on ω^2, a tendency exists for QII and Q0 to favor $+\omega_2$ and for QIV to favor $-\omega_2$ at the earliest times.

In the rotation-dominated QII regions, the dynamics of fluctuating **G** are dominated by reorientation by fluctuating ω. The associated spatial orientation of **G** is shown in Figs. 13(a), 13(b). At a very early time [St$=$0.5, Fig. 13(a)], high probabilty occurs for $|\theta_{\text{pitch}}|<45°$ with $-30°<\theta_{\text{yaw}}<-150°$. The significant $+\omega_2$ and $\pm\omega_1$ associated with these regions at this time act to reorient $\overline{G}_3$ (terms GR1, GR5) generating, respectively, $-G_1$ and $\pm G_2$ ($-30°<\theta_{\text{yaw}}<-150°$). Through this mechanism, the correlations $\langle\omega_2 G_1\rangle<0$ and $\langle\omega_1 G_2\rangle>0$ are established which lead to $\langle\omega_1 G_2-\omega_2 G_1\rangle>0$ (GR6, GR7). As indicated in (4.7), this results in the promotion of $+G_3$. By St$=$6 [Fig. 13(b)], $\theta_{\text{pitch}}\approx 70°$ indicating significant positive vertical fluctuations, $+G_3$. Gradient amplication by $S_{33}<0$ (GS3) acts to maintain this component. At the same time, since $\pm\omega_1$ is significant, reorientation of $+G_3$ gives rise to $\mp G_2$ (GR4). Accordingly, the distribution extends out towards $\theta_{\text{yaw}}=0°,\pm 180°$ [see arrows in Fig. 13(b)].

In the strain-dominated QIV regions, the dynamics of **G** are controlled by interaction with S although reorientation by fluctuating ω becomes important at later times. The orientation of **G** at St$=$0.5 [Fig. 13(c)] favors $\theta_{\text{yaw}}\approx 90°$ and $-40°<\theta_{\text{pitch}}<0°$. At early time, fluctuating **G** is generated through interaction of $\overline{G}_3$ with S, in particular, **G** is amplified along $\boldsymbol{e}_\gamma$ and attenuated along $\boldsymbol{e}_\alpha$ (GS2, GS4). This promotes $+G_1$ and $-G_3$ consistent with the orientations indicated in the jpd. During this time, **G** tends to orient near $\boldsymbol{e}_\gamma$ and $\mathbf{G}^2$ increases significantly due to the high magnitudes of compressive strain associated with this sample. However, at St$=$6 [Fig. 13(d)], the orientation of **G** shows the growing significance of reorientation by ω. The prevailing $+\omega_2$ and accompanying $\pm\omega_3$ act to reorient $+G_1$ to produce $-G_3$ (GR7) and $\pm G_2$ (GR3), respectively. The corresponding trends in the jpd are indicated by arrows in Fig. 13(d). Thus, although $|\mathbf{G}|$ is amplified by compressive strain, reorientation by ω remains significant in producing variations in the orientation of **G**.

As expected, the effects of both rotation and strain are important in Q0 regions. The corresponding orientation of **G** is given in Figs. 14(a), 14(b). At an early time [Fig. 14(a)], the peak in the jpd is associated with $-30°<\theta_{\text{yaw}}<-150°$ which indicates the presence of significant $-G_1$ and $\pm G_2$. As in QII, $+\omega_2$ and $\pm\omega_1$ predominate at early time and act to reorient $\overline{\mathbf{G}}_3$ generating $-G_1$ (GR1) and $\mp G_2$ (GR5). Since S^2 is significant in Q0, interaction of S and **G** is also important in establishing the initial fluctuations. The generated $-G_1$ is amplified along $\boldsymbol{e}_\gamma$. The peak in Fig. 14(a) essentially coincides with that of $\boldsymbol{e}_\gamma$ (not shown). In addition, amplification of $\overline{G}_3$ along $\boldsymbol{e}_\gamma$ (GS2, GS4), significant in QIV, results in the appearance of events in the upper left quadrant of the jpd. In time, the peak in the jpd develops towards $\theta_{\text{pitch}}=-90°$ with $0°<\theta_{\text{yaw}}<180°$ [indicated by arrows in Fig. 14(b)] which corresponds to $-G_3$ and $\pm G_2$. In Q0 regions, $+\omega_2$ becomes dominant and acts to reorient **G** giving rise to $+G_1$ and later $-G_3$ (GR2, GR7). The accompanying $\pm\omega_3$ results in $\pm G_2$ (GR3). Thus, as in QIV, although gradient amplification along $\boldsymbol{e}_\gamma$ is significant, the orientation of **G** tends to deviate from that of $\boldsymbol{e}_\gamma$ due to the influence of ω.

The spatial orientation of **G** associated with the total flow is shown in Figs. 14(c), 14(d). At an early time of St$=$0.5 [Fig. 14(c)], the jpd generally follows the S^--plane curve which corresponds to probable orientations for $\boldsymbol{e}_\gamma$ in the flow. Later in time [Fig. 14(d)], the orientation of **G** in the total flow is similar to that in QII [Fig. 13(b)]. As shown

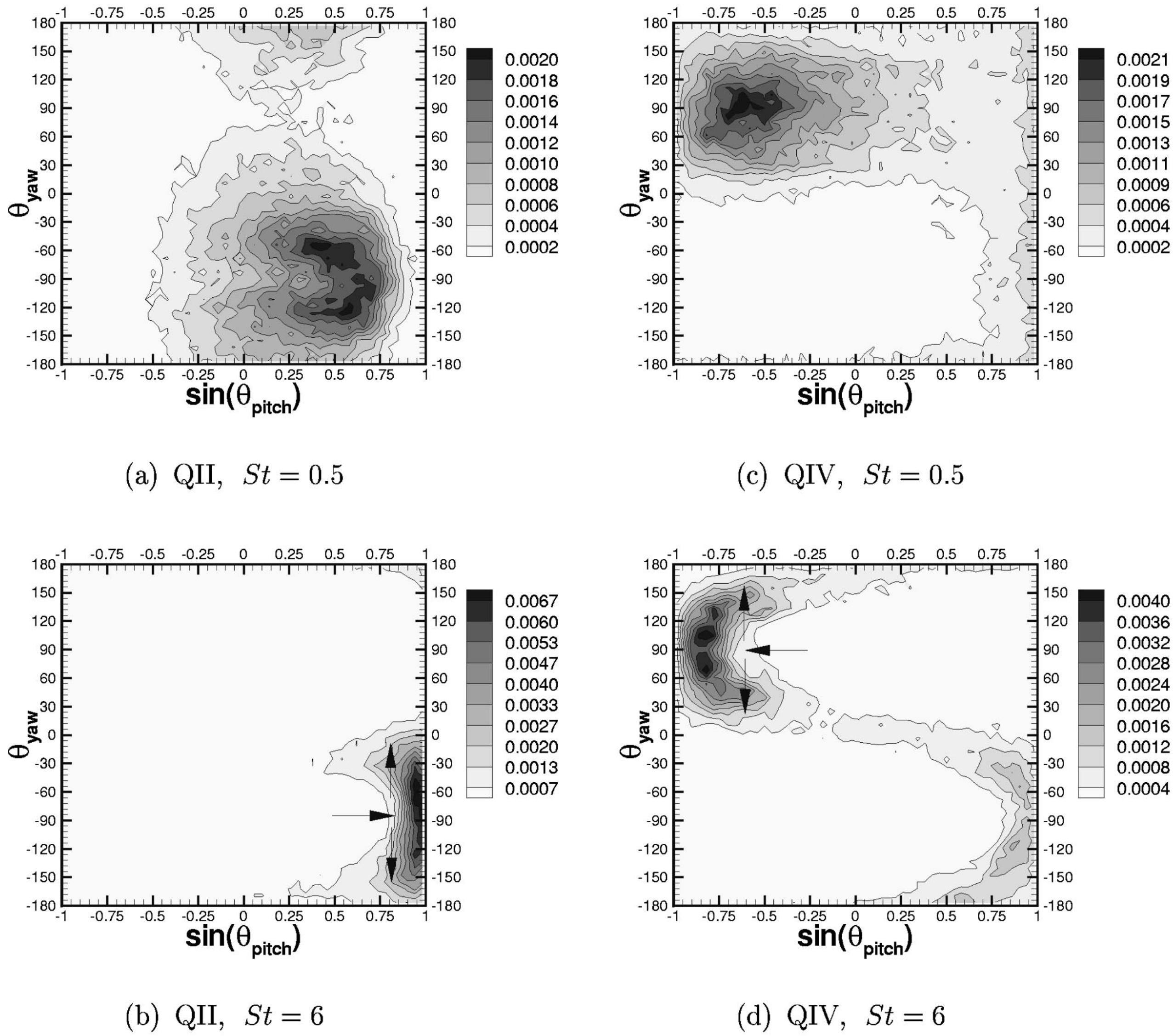

FIG. 13. Joint probability distributions indicating the angles of orientation ($\theta_{\text{pitch}}, \theta_{\text{yaw}}$) of G_i for Ri=0: (a) QII, St=0.5, (b) QII, St=6, (c) QIV, St=0.5, (d) QIV, St=6.

in Figs. 18(a) and 18(b), the evolution of the **G** components in the total flow generally follows that of QII. A secondary peak in the jpd appears to be associated with Q0 and QIV events [Figs. 14(b), 13(d)]. The orientation of passive **G** in the total flow is thus characterized by both rotation and strain events.

F. Active scalar gradient dynamics

In the presence of buoyancy, ρ is an active scalar and the dynamics of ω, S, and **G** represent a fully coupled system. In particular, density differences between adjacent particles are influenced by gravity with consequences on the flow. Two additional mechanisms are introduced in the dynamics of ω and S. The first is *baroclinic torque* which appears in the horizontal component equations for fluctuating ω (expressed here without the viscous terms),

$$\frac{D\omega_1}{Dt}=S_{1k}\omega_k+S_{12}\bar{\omega}_2+\bar{S}_{13}\omega_3\underbrace{-RiG_2} \tag{4.8}$$

$$\frac{D\omega_2}{Dt}=S_{2k}\omega_k+S_{22}\bar{\omega}_2\underbrace{+RiG_1} \tag{4.9}$$

The underbraced terms represent the fact that, in the presence of horizontal gradient fluctuations, i.e., $\pm G_1$ or $\pm G_2$, gravity will cause heavy particles to sink while adjacent lighter ones slide into their place thus generating a local rotational motion, i.e., baroclinic torque. The second mechanism is that of *differential acceleration* which appears in the evolution

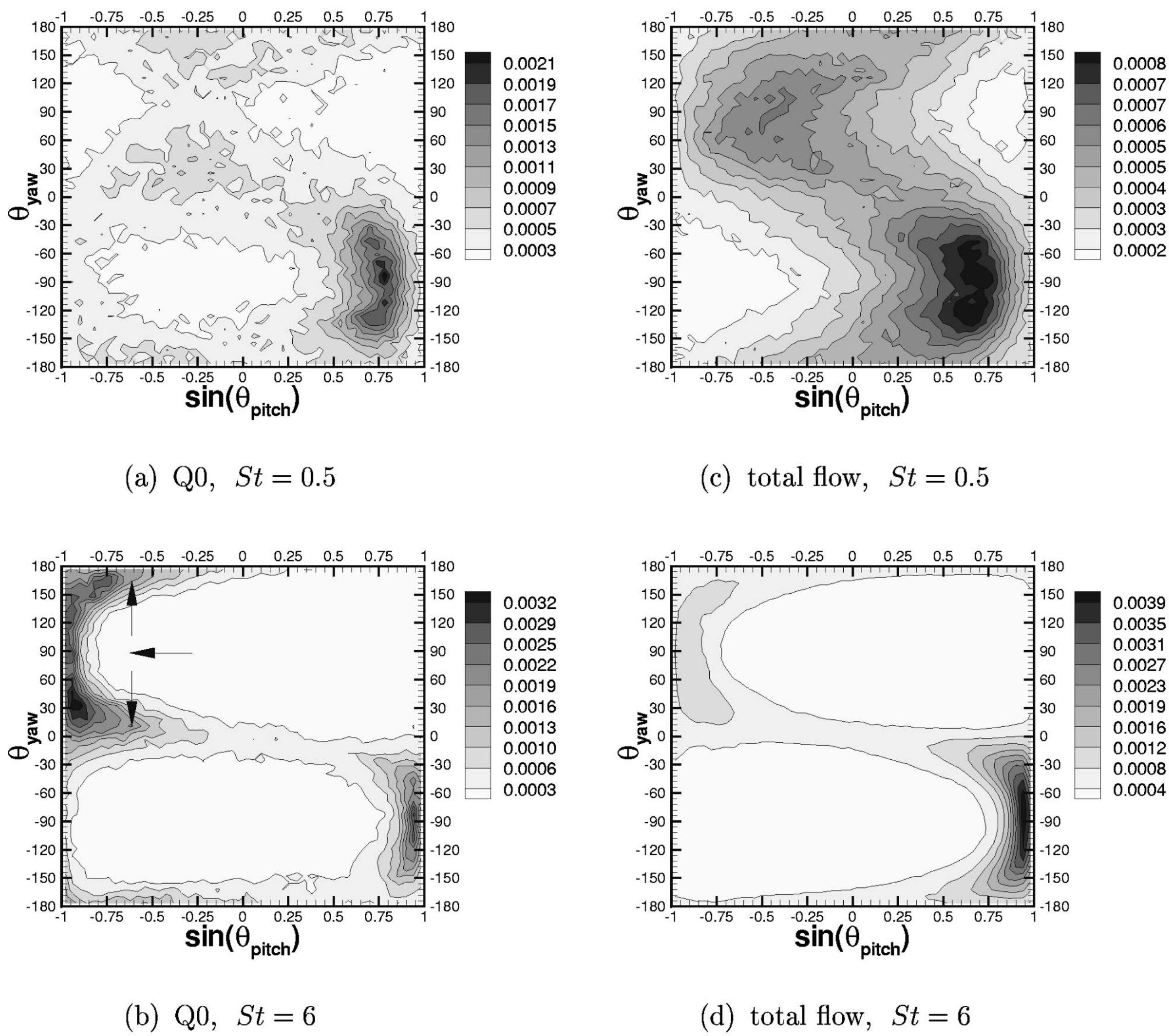

FIG. 14. Joint probability distributions indicating the angles of orientation ($\theta_{\text{pitch}}, \theta_{\text{yaw}}$) of G_i for Ri=0: (a) Q0, St=0.5, (b) Q0, St=6, (c) total flow, St=0.5, (d) total flow, St=6.

equation for a S_{3j} component of S (2.2), e.g., S_{33},

$$\frac{DS_{33}}{Dt} = -S_{33}{}^2 + \frac{\omega_1^2+\omega_2^2}{4} - \Pi_{33} \underbrace{-RiG_3} \qquad (4.10)$$

Physically, differential acceleration represents the enhancement of compressive straining when high density fluid occurs above that of low density, i.e., $+G_3$.

Early in the development of the flow (St<1, shear-dominated phase), the behavior of **G** is similar to that of the passive gradient since buoyancy effects have not had sufficient time to influence the small scales of the flow. The corresponding structure of **G** in each of the conditional samples as well as the total flow at St=0.5 is similar to those of NB [Figs. 13(a), 13(c), 14(a), 14(c)]. Beyond St=1, the flow enters the onset of buoyancy control phase and the behavior of HB begins to deviate from that of NB (see Fig. 18).

Figures 15(a) and 15(b) show the orientation of fluctuating **G** in the QII sample of HB at St=2 and St=6. As previously stated, at very early times (St=0.5, not shown), the behavior is similar to that in the passive case [Fig. 13(a)] and a prevalence of $-G_1$ and $\pm G_2$ is exhibited due to interaction of $\overline{G_3}$ with $+\omega_2$ and $\pm\omega_1$, respectively. However, as indicated in Eqs. (4.8)–(4.9), baroclinic torque will generate ω of opposite sign to that which gave rise to the corresponding G_i component. This promotes the correlations $\langle\omega_2 G_1\rangle>0$ (GR7) and $\langle\omega_1 G_2\rangle<0$ (GR5) in Eq. (4.7) which consequently give rise to $-G_3$ ($\theta_{\text{pitch}}<0$) as evidenced by the appearance of events in the upper left quadrant in Fig. 15(b) [not present in NB, Fig. 13(b)]. Thus, at early time, baroclinic torque tends to act as a sink for ω^2. As the flow develops and sufficient **G** is present, baroclinic torque may become a source of ω. In general, however, the direct interaction of baroclinic torque and reorientation of **G** by ω is characterized by an inherent negative feedback. This is fur-

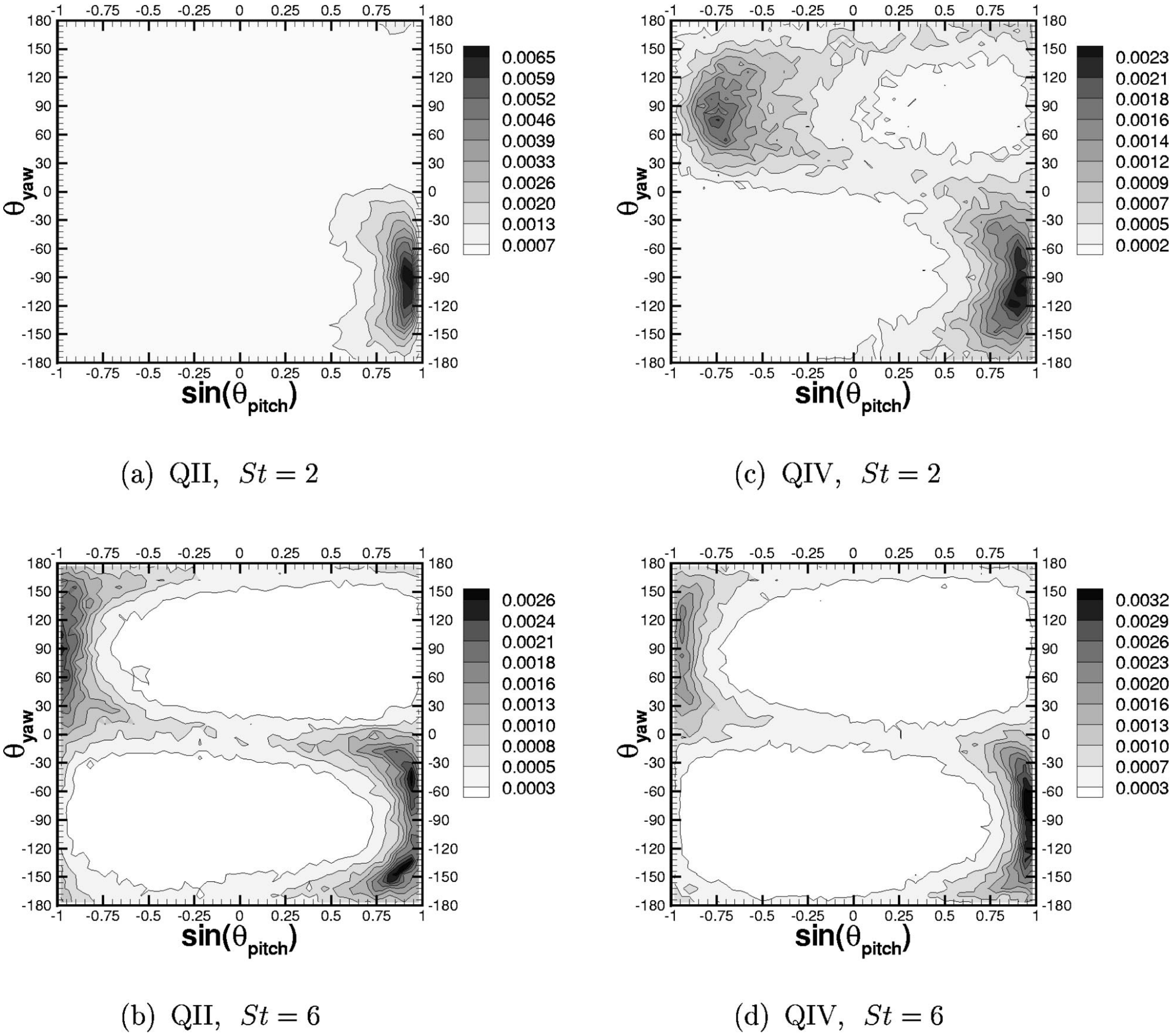

FIG. 15. Joint probability distributions indicating the angles of orientation ($\theta_{\text{pitch}}, \theta_{\text{yaw}}$) of G_i for Ri=1: (a) QII, St=2, (b) QII, St=6, (c) QIV, St=2, (d) QIV, St=6.

ther corroborated by additional simulations we have performed (not shown) in which initial scalar fluctuations (and associated **G**) are present. In these flows, although baroclinic torque acts as a source of ω^2 at early times, the inherent negative feedback emerges at later times and the behavior becomes similar to that of the HB flow presented here. In regards to differential acceleration effects, we note at St=2 [Fig. 15(a)], significant $+G_3$ develops as in the NB flow. As indicated by Eq. (4.10), $+G_3$ promotes negative S_{33}. In QII regions of NB, ω_3 is significant at early times and then decreases at later times due to the dynamics of ω and S [see Fig. 17(b)]. The strain component S_{33} tends to become negative. With buoyancy, $+G_3$ leads to an enhanced (greater probability) negative S_{33} which, consequently, results in an increased attenuation of ω_3. This is indicated in Fig. 10(f) which shows a higher θ_{pitch} for $\boldsymbol{e}_\gamma$. Although the tendency for negative S_{33} is also exhibited by the NB flow, differential acceleration establishes significant $S_{33}<0$ much earlier in the development of the HB flow. The combined action of baroclinic torque and differential acceleration (and consequent vortex contraction) thus lead to the observed predominance of horizontal ω in these regions [Fig. 7(d)] which correspond to horizontal spatial structures [Fig. 3(d)].

In general, high magnitude **G** is associated with high S^2 due to gradient amplification by compressive straining. As a result, baroclinic torque generation is significant in QIV and acts as a source for ω^2. The orientation of **G** in QIV is shown in Figs. 15(c), 15(d). At St=2 [Fig. 15(c)], two maxima are observed and indicate the presence of significant $+G_1, -G_3$ (upper left quadrant) and also $-G_1, +G_3$ (lower right quadrant). As in NB, interaction of $\overline{G}_3$ and S promotes $+G_1$ and $-G_3$ at early time. The presence of $+G_1$ generates $+\omega_2$ through baroclinic torque (4.9). The enhanced spanwise vorticity at early time [Fig. 7(c)] effectively impedes locally-induced rotation of $\boldsymbol{e}_\alpha$ and $\boldsymbol{e}_\beta$ by re-

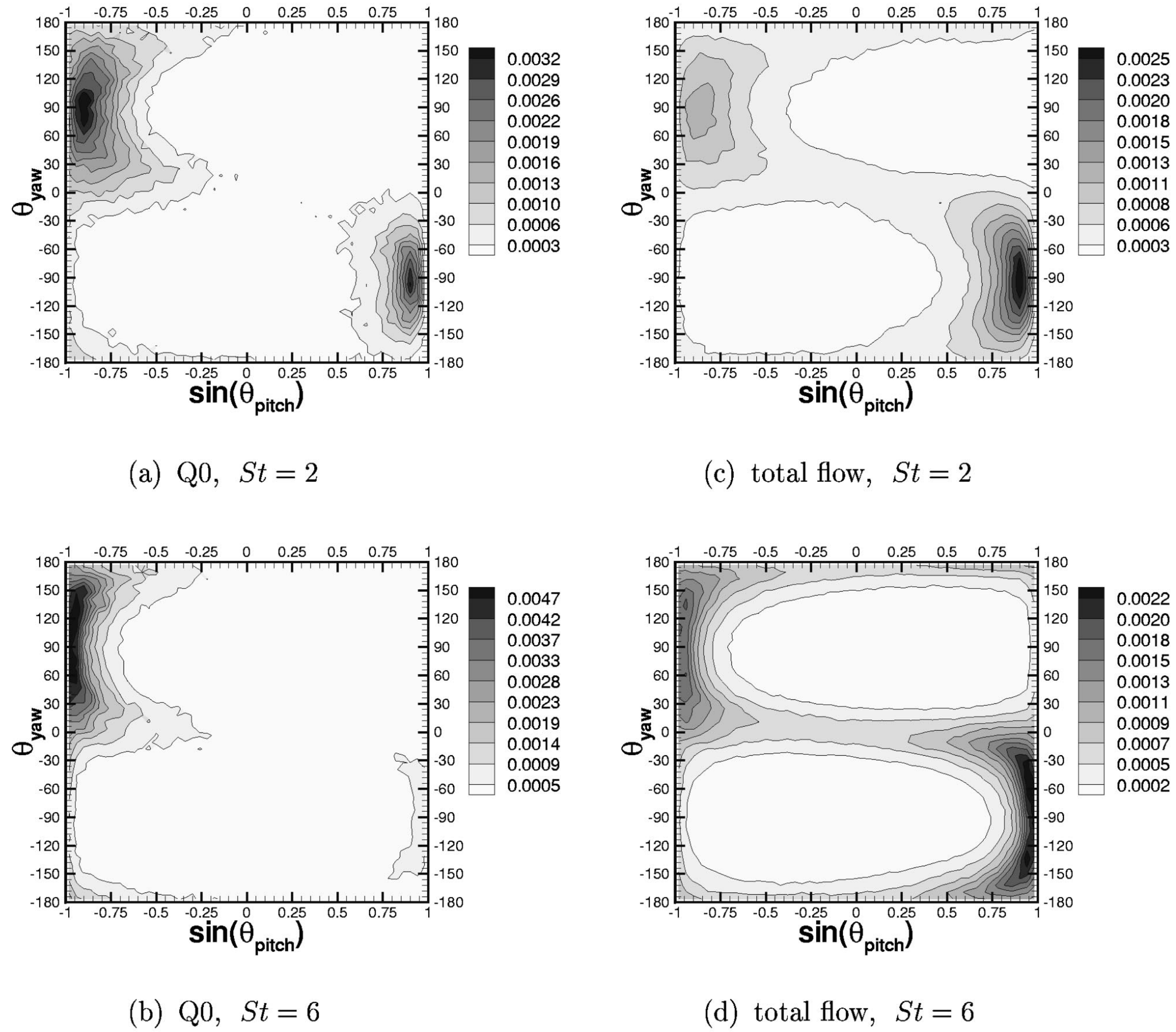

FIG. 16. Joint probability distributions indicating the angles of orientation ($\theta_{\mathrm{pitch}}, \theta_{\mathrm{yaw}}$) of G_i for Ri=1: (a) Q0, St=2, (b) Q0, St=6, (c) total flow, St=2, (d) total flow, St=6.

ducing the degree of misalignment of ω with the eigenvectors (4.4). This is evidenced in Figs. 12(d) and 12(e) where a reduction in the extent of rotation of the axes (as compared with NB) is observed. Note, in comparing the orientation of **G** in NB [Fig. 13(d)] and HB [Fig. 15(d)], there is greater probability for events with $\theta_{\mathrm{yaw}}<0$ and $\theta_{\mathrm{pitch}}>0$ (lower right quadrant). This is due to a positive feedback mechanism involving differential acceleration. At very early times, the jpd is similar to that in NB [Fig. 13(c)] and indicates some occurrence of $+G_3$. With buoyancy, $+G_3$ promotes $-S_{33}$ through differential acceleration (4.10). This leads to amplification of $+G_3$ [GS3, GS4 in Eq. (4.7)] which thereby establishes a positive feedback mechanism effective in maintaining $+G_3$. In NB, such a mechanism does not exist and there is less occurrence of $+G_3$ [Fig. 13(d)].

Figures 16(a) and 16(b) show the jpds for Q0 regions where rotation and strain are comparable. A key difference with Q0 in NB [Figs. 14(a) and 14(b)] is the earlier appearance of events in the upper left quadrant of the jpd ($\theta_{\mathrm{pitch}} <0°$). Recall that in NB at early time, amplification of $\overline{G_3}$ along $\boldsymbol{e}_\gamma$ promotes $+G_1$ and $-G_3$ and thus results in the appearance of events in the upper left quadrant of the jpd in Fig. 14(a). Prevailing $+\omega_2$ acts to reorient **G** which promotes $-G_3$ (GR7) and leads to the orientation in Fig. 14(b). In HB, the presence of $+G_1$ generates $+\omega_2$ through baroclinic torque. Since S^2 is also high in Q0, $\mathbf{G}^2$ is high and thus baroclinic torque is significant in this sample (comparable to QIV). This results in a dominant spanwise ω shown in Fig. 7(e) which, as in the case of QIV, impedes S axes rotation (Fig. 11). The reduction in S axes rotation will affect the subsequent evolution of ω. This may explain the difference in structure of these regions [Figs. 4(c), 14(d)] which do not exhibit the wavy feature observed in the NB flow [Figs. 4(a), 4(b)]. The **G** field also exhibits a more rapid appearance of $-G_3$ [Fig. 16(a)]. This $-G_3$ promotes $S_{33}>0$ through differential acceleration (4.10) and, as a consequence, there is a rapid decay in $|G_3|$ beyond St=2.

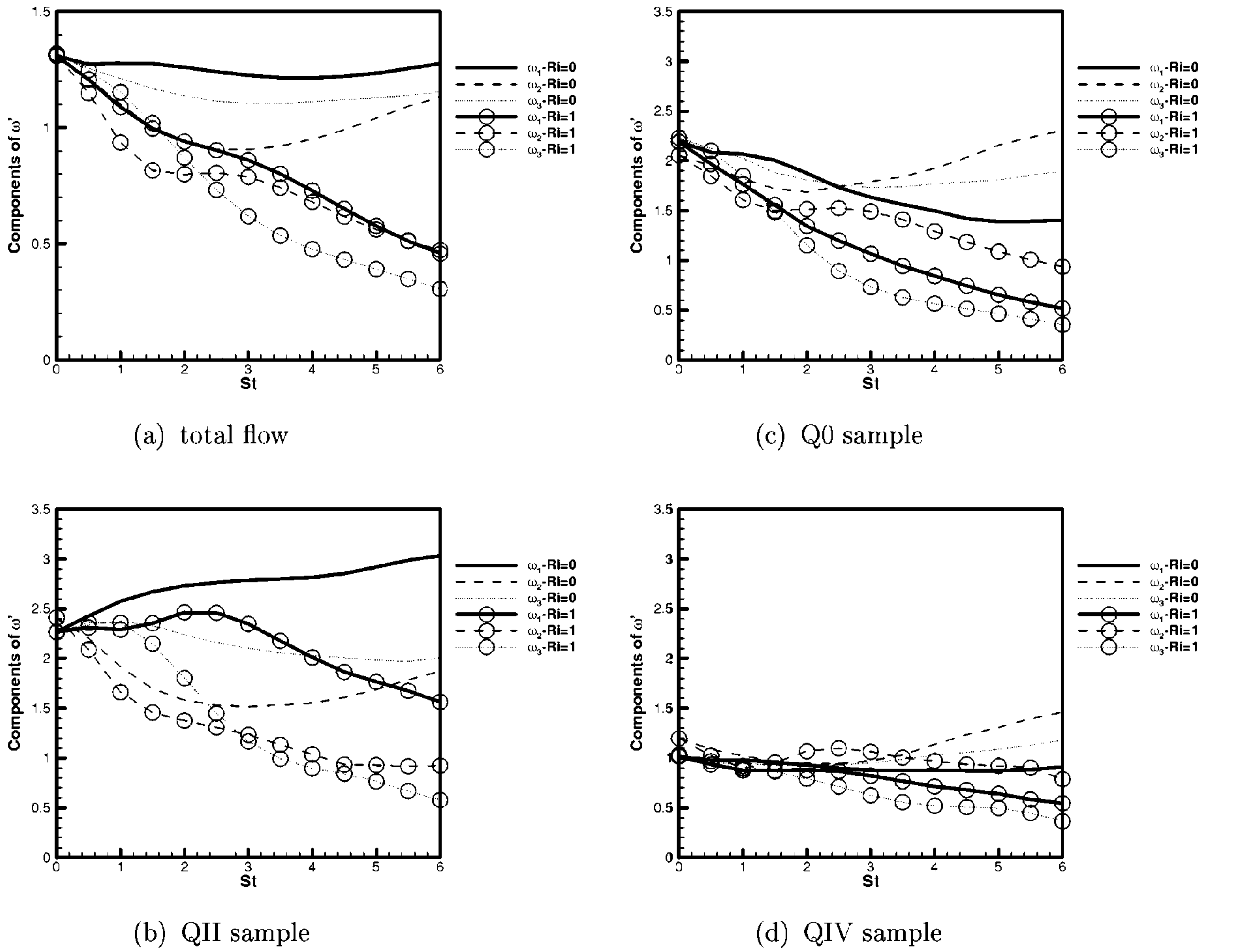

FIG. 17. Time evolution of the rms fluctuating vorticity ω' components for Ri=0 (plain lines) and Ri=1 (with ○): (a) total flow and (b) QII, (c) Q0, (d) QIV conditional samples.

The orientation of **G** for the total flow is shown in Figs. 16(c) and 16(d). In general, as in NB, the behavior of **G** depends on both rotation and strain events. In NB, the presence of the mean gradient and shear leads to a preference for $+G_3$. In HB, although $+G_3$ persists, $-G_3$ is also significant. The behavior of Q0 events appears to be more significant in HB as indicated by Fig. 16. Note that in HB, the jpd of **G** for the total flow exhibits a peak at $\theta_{\text{pitch}} \approx 80°$, indicating an even stronger preference for $+G_3$ with increasing stratification. This is consistent with the experimental measurements of Keller and Van Atta[24] which show gradients of temperature becoming increasingly vertical in the negative x_3 direction with increased stratification.

The above analysis is consistent with the time evolution of the rms components of ω and **G**. As discussed, the behavior of ω is generally described by QII and Q0 events. Figure 17 shows the evolution of ω for the total flow along with QII and Q0 samples. In the QII sample in NB [Fig. 17(b)], both ω_1 and ω_3 initially increase due to amplification by the mean extensional strain while ω_2 decreases. Beyond St=1, ω_1 continues to increase while ω_3 decreases. Later in time (St >4), ω_2 begins to increase due to further interaction of ω and S. In the Q0 sample in NB [Fig. 17(c)], the rms of all three components decay until time St=2. At time St=3, ω_2 begins to increase due to amplification of the mean vorticity and is accompanied by increasing ω_3. The development of the total flow generally follows that of QII with increasing contribution from Q0 as the flow develops in time.

In the HB case, behavior of ω_1 and ω_3 show competition between shear and buoyancy effects. In QII [Fig. 17(b)], ω_3 initially increases due to mean shear effects and then (St >1) drops rapidly due to the effects of differential acceleration. The initial amplification in ω_1 by mean strain is counteracted by baroclinic torque and, eventually, ω_1 exhibits a decay. In regards to ω_2, the initial decay is more rapid than in NB due to baroclinic torque which acts as a sink during this time. Later in time, ω_2 remains relatively constant as baroclinic torque may act as a source for ω_2 and the interaction of ω and S promotes this component. In Q0, ω_1 and ω_3 exhibit a continual decay in time. The component ω_2 initially decays until approximately St=1 at which time baroclinic torque generation and shear effects act to maintain this component for a short period of time [also observed in QIV, Fig. 17(d)]. As the flow develops, shear effects are reduced (recall S axes rotation is impeded). Beyond St=3, ω_2 proceeds to decay at a rate similar to that of the other two components.

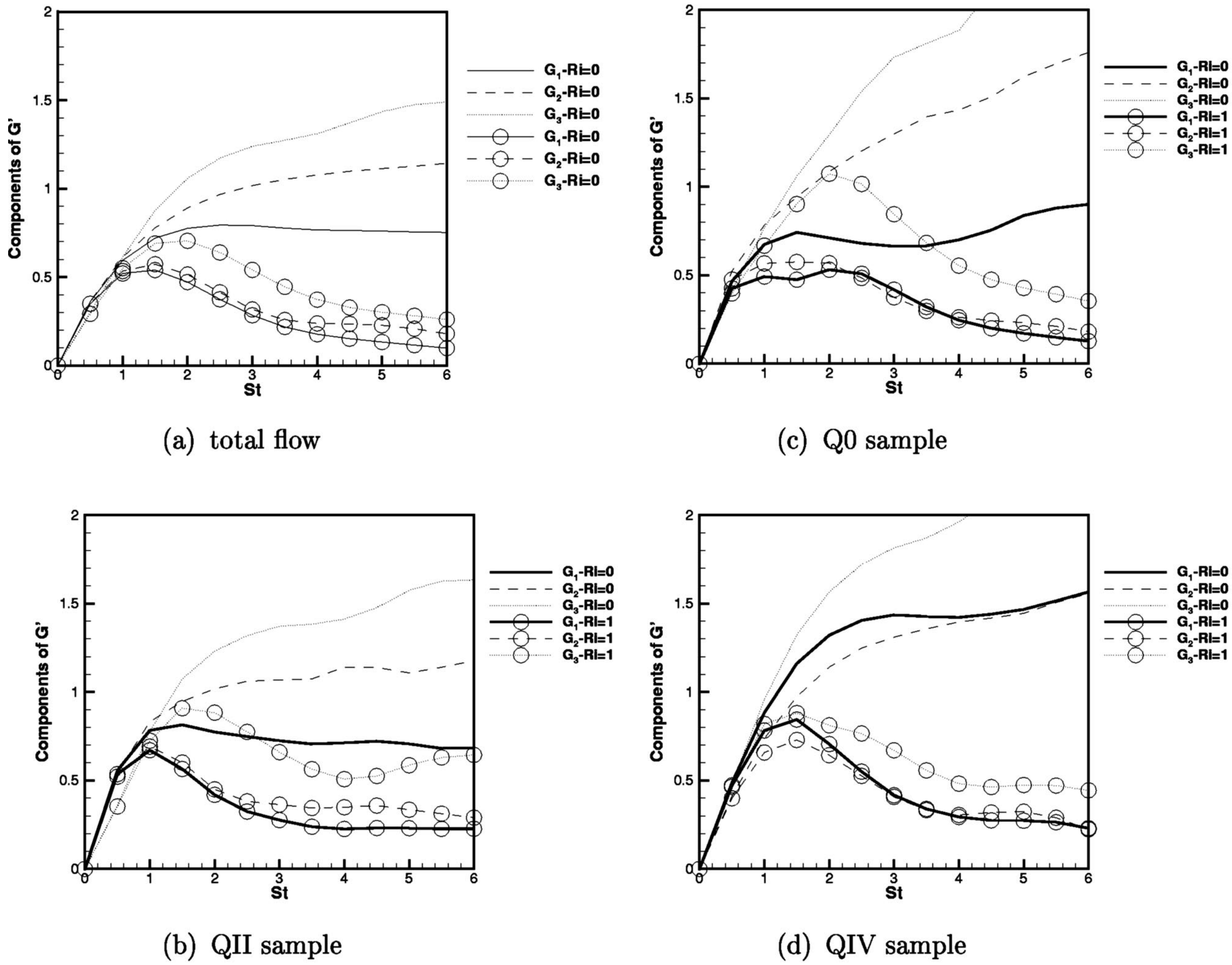

FIG. 18. Time evolution of the rms fluctuating scalar gradient G_i components for Ri=0 (plain lines) and Ri=1 (with ○): (a) total flow and (b) QII, (c) Q0, (d) QIV conditional samples.

The total flow behavior of HB [Fig. 17(a)] shows a predominance of ω_1 and ω_2 at later times which can be attributed to QII and Q0 events, respectively.

The evolution of the rms components of **G** is given in Fig. 18. In NB, G_3 dominates and exhibits the greatest rate of increase in high strain regions (Q0 and QIV). However, the overall behavior of the total flow appears more similar to that of QII. In HB, G_3 remains the dominant component. As discussed, beyond St=1, the behavior deviates from that in NB. Although G_3 continues to increase for a short period, beyond St=2, a decay in all three components is observed. Computed values of $\langle G_3^2\rangle/\langle G_1^2\rangle$ (not shown) show a more rapid growth rate in HB than in NB. Similar results have been observed in the experiments of Keller and Van Atta.[24] They conclude that the combination of shear and stable stratification, particularly for supercritical Ri, enhances the anisotropy of **G** compared to the action of shear or stratification alone.

The behavior of magnitudes in S is presented in terms of probability distributions of the eigenvalues (Fig. 19). As previously reported,[1–5] $\langle\beta\rangle>0$ in homogeneous turbulence. Furthermore, there is an increased probability of $\beta>0$ in regions of high amplitude S^2. Results for NB are in agreement. The total flow [Fig. 19(a)] shows $\langle\beta\rangle>0$ while the QIV sample [Fig. 19(a)] indicates $\beta>0$ for essentially all observations in the sample. In HB [Figs. 19(c) and 19(d)], the magnitudes of the eigenvalues are diminished and the structure of S is modified. The total flow distribution shows the peak in β to be nearly zero. In the QIV sample [Fig. 19(d)], although the distribution in β remains skewed to positive values, negative values occur. In general, the distributions become more symmetric in time. The nearly zero $\langle\beta\rangle$ is also indicated by the third invariant III which tends toward zero for all values of II [Fig. 2(b)]. The implication on the dynamics is a reduction in vortex stretching and associated energy transfer, and in S^2 production.

V. CONCLUSIONS

The structure and dynamics associated with the triadic interaction of vorticity ω, rate-of-strain S and scalar (density fluctuation) gradient **G** have been investigated in homogeneous sheared turbulence with uniform stable stratification. Although this flow is highly idealized, it contains two essen-

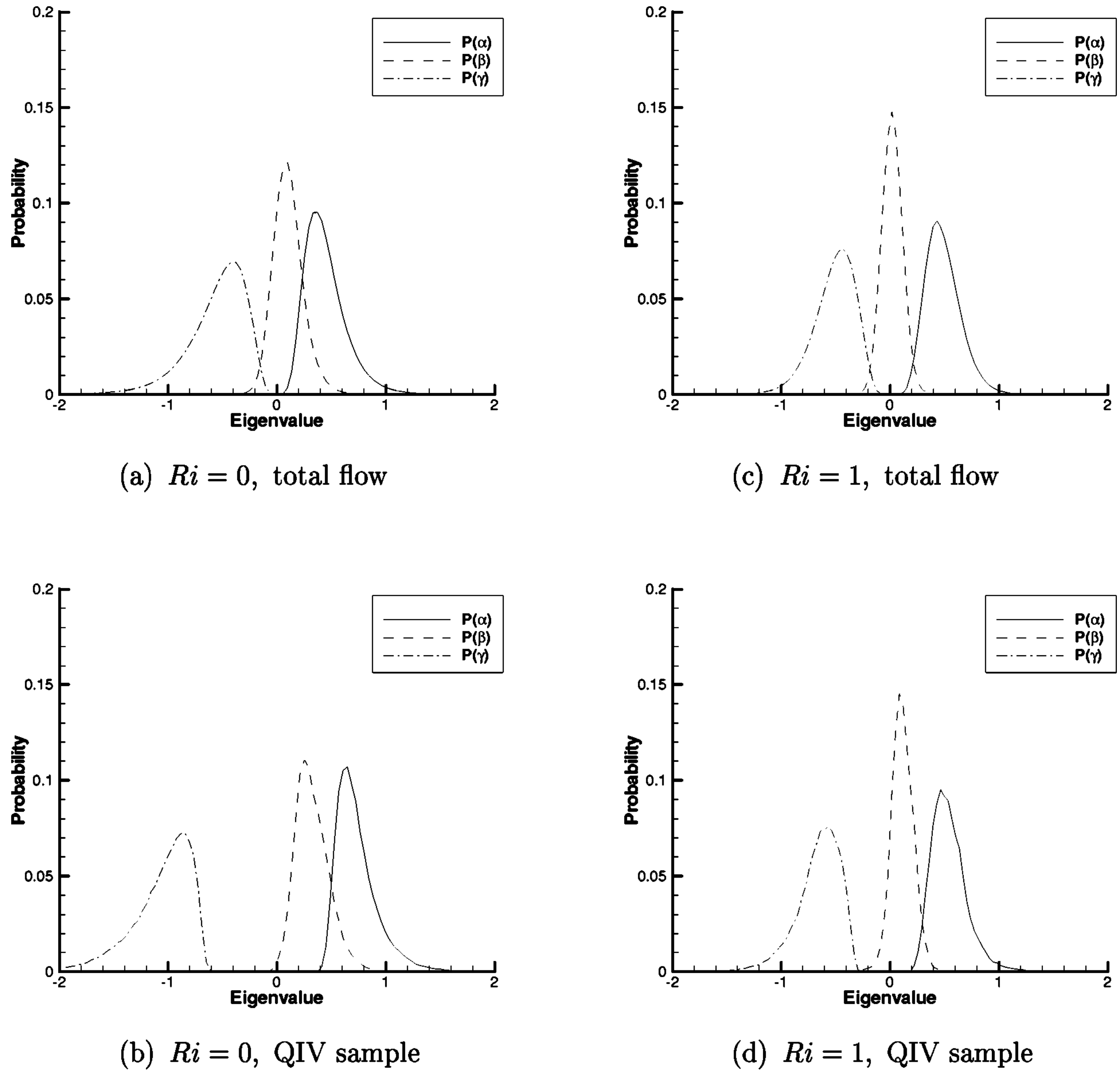

FIG. 19. Probability distributions of the principal eigenvalues of S, α, β, γ, at St=6: (a) Ri=0, total flow, (b) Ri=0, QIV sample, (c) Ri=1, total flow, (d) Ri=1, QIV sample (note that here, the eigenvalues are normalized by rms vorticity).

tial components, i.e., shear and stratification, which allow the study of some of the basic physics of stratified turbulent flows encountered in environmental and engineering applications. In the presence of mean shear and stratification, directional features in ω and S will influence **G**. With buoyancy, any preferential orientation in **G** will feedback on ω and S. The associated dynamics are complex with interacting mechanisms. To assist in the analysis, conditional sampling based on the invariants of the velocity gradient tensor is used. This serves to distinguish individual mechanisms by considering the relative significance of rotation vs strain. In general, the high amplitude conditional samples effectively capture the main features of the flow. Results illustrate the close relation between structure and dynamics in stratified sheared turbulence. The triadic interaction is described in terms of the direct coupling of primary mechanism pairs and influential secondary effects.

We first summarize the basic mechanisms present in the flow without buoyancy (NB), in which one-way coupling exists between the flow and scalar fields. The interaction of ω and S, effectively described in the principal strain basis, are influenced by the presence of mean ω and S. Initial stretching of fluctuating ω by mean extensional strain and the presence of mean vorticity establish a predominant misalignment of ω with respect to the principal axes of S. The associated locally-induced rotation of the S axes leads to preferred orientations in ω and S. The behavior of passive **G** is controlled by ω and S. In rotation-dominated QII regions, the behavior of **G** involves initial generation through reorientation of $\overline{G_3}$ by the prevailing ω. Further development leads to significant $+G_3$ in these regions. In strain-dominated QIV regions, fluctuating **G** is established by S. Gradient amplification by compressive straining is significant and results in high $\mathbf{G}^2$. Eventually, however, reorientation of $\mathbf{G}$ by ω becomes signficant and controls the direction of $\mathbf{G}$. In Q0 regions, effects of both rotation and strain are important in the behavior of $\mathbf{G}$. Overall, results indicate that the observed preferential orientation of $\mathbf{G}$ is established primarily by the prevailing ω in the flow.

In the presence of buoyancy (HB), $\mathbf{G}$ feeds back on ω and S through the mechanisms of baroclinic torque and differential acceleration. At early time (shear-dominated flow), the behavior is similar to the nonbuoyant flow. As the flow develops and enters the onset of buoyancy control phase, active $\mathbf{G}$ dynamics become apparent. In QII regions, an inherent negative feedback between baroclinic torque and reorientation of $\mathbf{G}$ by ω is revealed. This causes baroclinic torque to act as a sink which promotes decay of ω^2. The prevalence of $+G_3$ in QII regions, established by the interaction of $\mathbf{G}$ and ω in the presence of mean shear and stratification, enhances vertical compressive strain through differential acceleration which consequently attenuates ω_3 through vortex contraction. The combined effects of an enhanced attenuation of ω_3 and the maintenance of ω_1 and ω_2 by shear and baroclinic torque result in a predominance of horizontal vorticity. This is physically manifested as a collapse in vortex structures in the flow. In regions where S^2 is significant (Q0 and QIV), magnitudes of $\mathbf{G}$ tend to be high and baroclinic torque is more significant than in QII. Due to the intrinsic directionality of baroclinic torque, the generated ω acts to impede S axes rotation. In Q0, the orientation of the eigenvectors of S remain near those of the imposed mean shear. The presence of significant $\pm G_3$ in high S^2 regions results in differential acceleration. In the strain-dominated QIV regions, a positive feedback between differential acceleration and gradient amplification by compressive straining occurs and promotes persistent vertical $\mathbf{G}$. In the overall flow, the magnitudes of the strains are reduced and the structure of S is altered. The strong tendency for $\beta > 0$, observed in nonbuoyant flow, is diminished with buoyancy. As a result, vortex stretching and production of S^2 are reduced. The associated development of the third invariant III towards zero suggests two dimensionalization of the local flow.

ACKNOWLEDGMENTS

The authors are indebted to the University of California, San Diego for support for this research. K. K. N. gratefully acknowledges her support through the Hellman Fellows Program.

[1]R. M. Kerr, ''Higher-order derivative correlations and the alignment of small-scale structures in isotropic numerical turbulence,'' J. Fluid Mech. **153**, 31 (1985).
[2]W. T. Ashurst, A. R. Kerstein, R. M. Kerr, and C. H. Gibson, ''Alignment of vorticity and scalar gradient with strain rate in simulated Navier–Stokes turbulence,'' Phys. Fluids **30**, 2343 (1987).
[3]Z.-S. She, E. Jackson, and S. A. Orszag, ''Structure and dynamics of homogeneous turbulence: Models and simulations,'' Proc. R. Soc. London, Ser. A **434**, 101 (1991).
[4]G. R. Ruetsch and M. R. Maxey, ''Small-scale features of vorticity and passive scalar fields in homogeneous isotropic turbulence,'' Phys. Fluids A **3**, 1587 (1991).
[5]K. K. Nomura and S. E. Elghobashi, ''Mixing characteristics of an inhomogeneous scalar in isotropic and homogeneous sheared turbulence,'' Phys. Fluids **4**, 606 (1992).
[6]A. Tsinober, E. Kit, and T. Dracos, ''Experimental investigation of the field of velocity gradients in turbulent flows,'' J. Fluid Mech. **242**, 169 (1992).
[7]S. Douady, Y. Couder, and M. E. Brachet, ''Direct observation of the intermittency of intense vorticity filaments in turbulence,'' Phys. Rev. Lett. **67**, 983 (1991).
[8]J. Jimenez, A. A. Wray, P. G. Saffman, and R. S. Rogallo, ''The structure of intense vorticity in isotropic turbulence,'' J. Fluid Mech. **255**, 65 (1993).
[9]M. M. Rogers and P. Moin, ''The structure of the vorticity field in homogeneous turbulent flows,'' J. Fluid Mech. **176**, 33 (1987).
[10]M. Tanaka and S. Kida, ''Characterization of vortex tubes and sheets,'' Phys. Fluids A **5**, 2079 (1993).
[11]E. Villermaux, B. Sixon, and Y. Gagne, ''Intense vortical structures in grid-generated turbulence,'' Phys. Fluids **7**, 2008 (1995).
[12]K. K. Nomura and G. K. Post, ''The structure and dynamics of vorticity and rate of strain in incompressible homogeneous turbulence,'' J. Fluid Mech. **377**, 65 (1998).
[13]S. Kida and M. Tanaka, ''Dynamics of vortical structures in a homogeneous shear flow,'' J. Fluid Mech. **274**, 43 (1994).
[14]T. Gerz, J. Howell, and L. Mahrt, ''Vortex structures and microfronts,'' Phys. Fluids **6**, 1242 (1994).
[15]K. K. Nomura and P. J. Diamessis, ''The interaction of vorticity and rate of strain in homogeneous sheared turbulence,'' Phys. Fluids **12**, 846 (2000).
[16]A. Fincham, T. Maxworthy, and G. Spedding, ''Energy dissipation and vortex structure in freely decaying, stratified grid turbulence,'' Dyn. Atmos. Oceans **23**, 155 (1996).
[17]T. Gerz, in *Evolution of coherent vortex structures in sheared and stratified homogeneously turbulent flows*, Eighth Symposium on Turbulent Shear Flows (Munich, Germany, 1991).
[18]T. Gerz, in *Turbulence and Coherent Structures*, Turbulence 89: Organized structures and turbulence in fluid mechanics (Grenoble, France, 1991), pp. 449–468.
[19]Y. Kimura and J. R. Herring, ''Diffusion in stably stratified turbulence,'' J. Fluid Mech. **328**, 253 (1996).
[20]S. E. Holt, J. R. Koseff, and J. H. Ferziger, ''A numerical study of the evolution and structure of homogeneous stably stratified sheared turbulence,'' J. Fluid Mech. **237**, 499 (1992).
[21]A. Majda and M. J. Grote, ''Model dynamics and vertical collapse in decaying strongly stratified flows,'' Phys. Fluids **9**, 2932 (1997).
[22]A. D. Leonard and J. C. Hill, ''Mixing and chemical reaction in sheared and nonsheared homogeneous turbulence,'' Fluid Dyn. Res. **10**, 273 (1992).
[23]T. Gerz and U. Schumann, ''A possible explanation of countergradient fluxes in homogeneous turbulence,'' Theor. Comput. Fluid Dyn. **8**, 169 (1996).
[24]K. H. Keller and C. W. Van Atta, ''An experimental investigation into the vertical temperature structure of homogeneous stratified shear turbulence,'' J. Fluid Mech. (submitted).
[25]T. Gerz, U. Schumann, and S. Elghobashi, ''Direct simulation of stably stratified homogeneous turbulent shear flows,'' J. Fluid Mech. **200**, 563 (1989).
[26]V. Eswaran and S. B. Pope, ''An examination of forcing in direct numerical simulation of turbulence,'' Comput. Fluids **16**, 257 (1988).
[27]F. Jacobitz, ''Direct numerical simulation of turbulent stratified shear flow,'' Ph.D. dissertation, University of California, San Diego, 1998.
[28]F. Jacobitz, S. Sarkar, and C. Van Atta, ''Direct numerical simulations of the turbulence evolution in a uniformly sheared and stably stratified flow,'' J. Fluid Mech. **342**, 231 (1997).
[29]C. H. Gibson, in *Marine Turbulence*, edited by J. C. T. Nihoul (Elsevier, New York, 1980), pp. 221–258.
[30]C. H. Gibson, ''Internal waves, fossil turbulence and composite ocean microstructure spectra,'' J. Fluid Mech. **168**, 89 (1986).
[31]E. Itsweire, J. Koseff, D. A. Briggs, and J. H. Ferziger, ''Turbulence in stratified shear flows: Implications for interpreting shear-induced mixing in the ocean,'' J. Phys. Oceanogr. **23**, 1508 (1992).
[32]D. C. Stillinger, K. H. Helland, and C. W. Van Atta, ''Experiments on the transition of homogeneous turbulence to internal waves in a stratified

fluid,'' J. Fluid Mech. **131**, 91 (1983).
[33] R. Betchov, ''An inequality concerning the production of vorticity in isotropic turbulence,'' J. Fluid Mech. **1**, 497 (1956).
[34] B. J. Cantwell, ''On the behavior of velocity gradient tensor invariants in direct numerical simulations of turbulence,'' Phys. Fluids A **5**, 2008 (1993).
[35] P. Vieillefosse, ''Internal motion of a small element of fluid in an inviscid flow,'' Physica A **125**, 150 (1984).